RESEARCH ARTICLE

WILEY

Experimental study of the wake interaction between two vertical axis wind turbines

Ming Huang [ORCID] | Yugandhar Vijaykumar Patil | Andrea Sciacchitano | Carlos Ferreira

Aerodynamics, Wind Energy, Flight Performance & Propulsion Department, Faculty of Aerospace Engineering, Delft University of Technology, Delft, The Netherlands

Correspondence

Ming Huang, Aerodynamics, Wind Energy, Flight Performance & Propulsion Department, Faculty of Aerospace Engineering, Delft University of Technology, Kluyverweg 1, 2629 HS Delft, The Netherlands.
Email: m.huang-1@outlook.com

Abstract

Wakes and wake interactions in wind turbine arrays diminish energy output and raise the risk of structural fatigue; hence, comprehending the features of rotor–wake interactions is of practical relevance. Previous studies suggest that vertical axis wind turbines (VAWTs) can facilitate a quicker wake recovery. This study experimentally investigates the rotor–wake and wake–wake interaction of VAWTs; different pitch angles of the blades of the upwind VAWT are considered to assess the interactions for different wake deflections. With stereoscopic particle image velocimetry, the wake interactions of two VAWTs are analysed in nine distinct wake deflection and rotor location configurations. The time-average velocity fields at several planes upwind and downwind from the rotors are measured. Additionally, time-average loads on the VAWTs are measured via force balances. The results validate the rapid wake recovery and the efficacy of wake deflection, which increases the available power in the second rotor.

KEYWORDS

particle image velocimetry, vertical axis wind turbines, wake interaction

1 | INTRODUCTION

The interaction between wind turbine wakes and downwind rotors is one of the most crucial issues resulting in power losses in a wind farm. Downwind turbines operating in the wakes of upwind ones suffer from a decelerated and highly turbulent inflow, thus extracting less kinetic energy and enduring more severe fatigue loads. To alleviate the wake interaction effects, ample interturbine space and wake steering techniques are required for a wind farm of horizontal axis wind turbines (HAWT).[1,2] However, compared to the "optimal" wind turbine spacing, which could be as large as 15 diameters in infinitely large wind farms,[3–5] the limitation of site resources and the increasing demand for power production often lead to a smaller interturbine distance of 3 to 8 diameters.[6] This in turn intensifies the wake interaction in a wind farm.

Compared to HAWTs, vertical axis wind turbines (VAWTs) are less susceptible to the inflow direction and turbulence,[7] allowing for closer deployments without significantly deteriorating the performance of individual turbines. Moreover, reduced interturbine spacing of VAWTs has been identified as promising in increasing the wind farm power density. That is attributed to a faster wake recovery rate,[8] which has been confirmed both experimentally[9] and numerically.[10] In fact, to further increase the power density of an array of VAWTs, the wake steering concept has been adapted from HAWTs. A fixed blade pitch of VAWT is an easy and effective approach to deflect and deform the wake, without any additional complexity in the manufacturing of the turbine.[11] The simplified mechanics means lower construction cost, which is beneficial to reducing the cost of power generation.

The wake characteristics of isolated VAWTs have been extensively investigated experimentally. Tescione et al[12] carried out stereoscopic particle image velocimetry (PIV) measurements in the near wake of a VAWT, emphasising the interaction of tip vorticity generated upwind and downwind of the rotor. Ryan et al[13] adopted magnetic resonance velocimetry (MRV) to measure the averaged three-dimensional flow field behind a VAWT, and reported a pair of counter-rotating vortices dominating the wake flow topology. Araya et al[14] documented the similarity between the wake of a VAWT and a circular cylinder via planar-PIV. Rolin and Porté-Agel[9] examined the kinetic energy and momentum recovery of a small-scale VAWT in boundary layer flow by means of stereoscopic PIV, confirming that the counter-rotating vortex pairs are responsible for a faster recovery. Very recently, Wei et al[15] used 3D particle tracking velocimetry (PTV) to measure the wake of full-scale VAWTs, investigating the effect of blade geometries on the near wake structure. Huang et al[11] proposed a qualitative model to describe the relationship between blade loading and wake deflection. The model was verified via stereo-PIV measurements covering the near and far wake regions of isolated VAWTs with different pitch angles. Apart from revealing the physics in the wakes of VAWTs, there are studies on isolated VAWTs (e.g., previous works[16,17]) contributing to validating numerical simulations and analytical models.[18]

In a previous work from the authors,[11] isolated VAWTs have been shown to significantly redistribute the available wind power in the wake and manifest a quicker wake recovery rate via pitched blades. However, the effect of the wake deflection and deformation on downwind wind turbines was only hinted at and not assessed.

Of the few experimental studies on the wake of VAWT arrays, most have focused on the synergistic effect of VAWT clusters,[8,19−22] which is a kind of rotor–wake interaction. The synergistic effect occurs when multiple H-type VAWTs are placed close enough; in this condition, the performance of each one can be increased. Brownstein et al[22] measured the flow field surrounding a pair of scaled VAWTs with 3D-PTV, concluding that the increased performance is related to the bluff-body acceleration of the flow velocity around the turbines.

On the other hand, only a few studies have been performed on the wake–wake interaction of VAWTs, of which the majority are based on numerical simulations. Among these studies, the wake of VAWTs placed abreast are mostly investigated.[23−25] A minority has touched upon the wake interaction between upwind and downwind VAWTs or in tandem.[26−28] Likewise, field tests and experiments on VAWT wake interactions are rare. Kinzel et al[29] investigated the wake of a VAWT array under natural wind conditions, finding the similarity to the wake of a plant or urban canopy. Craig et al[30,31] examined the flow characteristics of an array of rotating cylinders via planar-PIV, especially the wake recovery enhanced by the vertical flows, indicating a potential analogy to VAWT arrays.

The wake–wake interaction is a critical consideration, especially for wind farm design, where the wakes of upwind wind turbines hit on the downwind ones and thus affect the overall momentum deficit, turbulence intensity fields and energy recovery rate.[32−34] Modelling the wake interactions via superposition models has been a practical technique to estimate multiple wake effects in wind farms.[35−37] Nevertheless, these models are subject either to oversimplified governing equations such as linear superposition or to the ill-defined superposition of turbulence fields.[38,39] Therefore, inspecting the momentum and turbulence distribution under the wake interaction has been of increasing interest for HAWTs (e.g., previous studies[37,40,41]), and it would be of similar interest for that of VAWTs, as the wind energy industry is seeing a potential boost of offshore VAWT farms due to their advantages in floating environments.[42,43]

Hence, experimental investigation on the wake interaction of VAWTs located upwind and downwind is desirable. This work investigates the wake interactions of VAWTs placed inline and with offset employing stereo-PIV, focusing on whether the wake deflection of VAWT gives more energy to an array configuration. In doing so, the upwind VAWT is set to vary the constant pitch angle of the blades to deflect its wake. Additionally, an in-house designed force balance system is adopted to quantify the averaged thrusts on the VAWTs, thus assessing the turbines' ability to extract momentum from the wind.

The remainder of the article is organised as follows. The methodology, the experiment apparatus and the cases examined are introduced in Section 2. Then, a section of results and discussion follows (Section 3), where an overview of the wake produced by the upwind VAWT with different fixed blade-pitch-angles is provided first as the control group. Second, the time-averaged thrust performance and wake properties of the interaction groups, together with a discussion on the available power behind the downwind VAWT, are presented. Finally, the key findings of this work are summarised in Section 4.

2 | EXPERIMENTAL METHODOLOGY

2.1 | Wind tunnel facility

The experiments are undertaken in the Open-Jet Facility (OJF) of the TU Delft Aerodynamics Laboratories. The OJF features a contraction ratio of 3:1 and an open exit of 2.85 m $\times$ 2.85 m. The stable free-stream, which is not affected by the development of the jet shear layer,[44] contracts with a 4.75° semiangle, resulting in an effective test area around 2.35 m $\times$ 2.35 m at 3 m behind the exit. The test wind speed is $U_\infty = 5\,\mathrm{ms}^{-1}$, with a free-stream turbulence intensity lower then 2% within the test region (see Lignarolo et al.[45]).

2.2 | The VAWT model

The scaled VAWT model is in-house designed, H-type, with a rotor size of 30 cm × 30 cm.[46] The two straight blades are made of aluminium, and the airfoil of the blades is NACA0012, with a chord length of 0.03 m. The solidity of the model is 0.2. The blades are connected to the tower with a pair of dedicated struts; the cross-section profile of the latter on the blade side is NACA0012 and transits to an ellipse with a thickness of 12% on the tower side, to reduce the drag and flow separation. The blades and the struts are connected with two pairs of bolts, allowing for a quick release and adjusting the fixed pitching angle; a pair of 3D printed adaptors are used to adjust the pitch angle (see Figure 1A). The pitch convention is presented in Figure 1B, with pitching towards the tower as positive, and vice versa. The rotor is driven by a brushless motor: *MAXON* EC 90 flat, and the motor is controlled by a *ESCON* 50/5 control module. A flexible coupling is used to filter out small vibrations in consideration of the misalignment due to machining accuracy. The locators at four feet are used to mount the entire VAWT model onto the balance system.

2.3 | The three-component force balance

An in-house designed and constructed three-component balance is employed for the load measurement. The balance is able to measure the streamwise and lateral forces. It consists of load cells (type: KD40s, max range ±50N, max error: ⩽0.1%), with two of them measuring the streamwise force (drag/thrust) while the other one measuring the lateral force. The overall uncertainty of the force measurement is of the same level as the load cells, provided that the flexural rods are aligned with the lift and the drag. As illustrated in Figure 1C, the load cells have one side attached to a stable aluminium frame directly and the other side to a platform via a dedicated flexural rod. The platform is suspended with four steel strings connected to the aluminium frame. The combination of the strings and the load cells prevents rotation caused by torque. The flexural rods are designed to solely transmit forces along its span-wise to prevent transmitting a moment and thus improve the measurement accuracy. The assembly was designed to tolerance levels of ±0.05 to ±0.15 mm. Additionally, four positioning holes are used to precisely centre the VAWT on the platform.

2.4 | Stereoscopic particle image velocimetry

The velocity fields in the wake of the VAWTs were obtained with stereoscopic PIV, which measures three velocity components within two-dimensional planes. A Quantel *Evergreen* double-pulsed Nd:YAG laser produced pulses with 200-mJ energy at a wavelength of 532 nm within a laser sheet of approximately 3 mm width. A *SAFEX* smoke generator released water-glycol seeding particles of average 1 μm diameter. The seeding particles were imaged by two LaVision's Imager sCMOS cameras in successive cross-sections of the wake. The cameras have an image resolution of 2560 px × 2160 px, a pixel pitch of 6.5 μm/px; they were coupled with 50-mm lenses with a numerical aperture of 4. We placed the cameras about 2.2 m away from the centre of the laser sheet with a stereoscopic angle of 90°, resulting in a camera field of view (FOV) about 80 × 55 cm^2, a magnification factor of 0.026, and a digital image resolution of 3.9 px/mm.

①VAWT rotor ②brushless motor ③motor controller ④flexible coupling ⑤locators ⑥pitch adapter
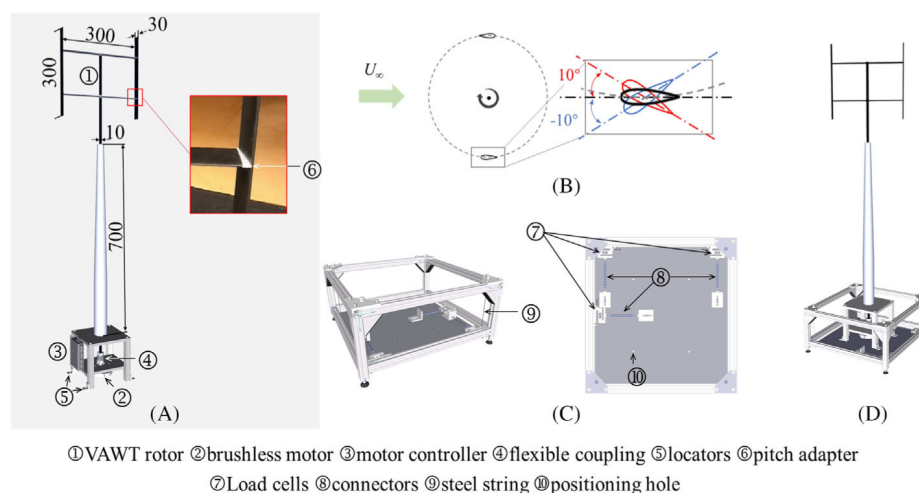⑦Load cells ⑧connectors ⑨steel string ⑩positioning hole

FIGURE 1 (A) Schematic of the VAWT model, dimensions in mm; (B) convention of the blade pitch; (C) an in-house designed three component balance system; (D) assembly of the VAWT and the balance.

To translate the PIV system precisely, a traversing system is employed whereby the stereo-PIV setup is mounted on, enabling navigation from 0.3 m to 3 m behind the wind tunnel exit with a step of 0.3 m. An overview of the experimental setup is shown in Figure 2. As illustrated, there is no ground effect accounted for in the measurement.

2.5 | Cases description

Measurements of the isolated VAWT at three different pitch angles ($-10°$, $0°$, and $10°$) compose the control group. As illustrated in Figure 3, measurements take place at 10 planes behind the turbine with $1D$ spacing, being $D = 30$ cm the VAWT diameter. These measurements are used

(A)   (B)

①camera 1 ②camera 2 ③*Evergreen* laser ④force balance ⑤laser sheet
⑥stereo-FoV ⑦traversing system ⑧wind tunnel exit ⑨VAWT1 ⑩VAWT2
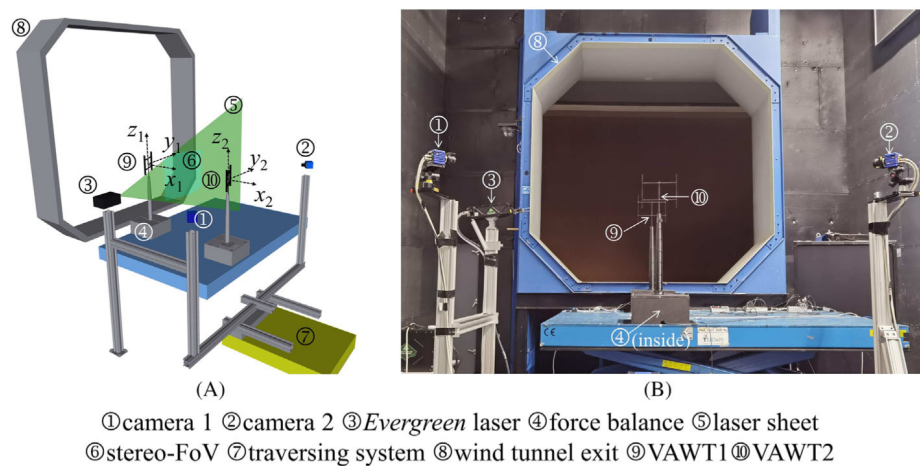
FIGURE 2   (A) Schematic of the experimental setup; (B) a snapshot of the setup.
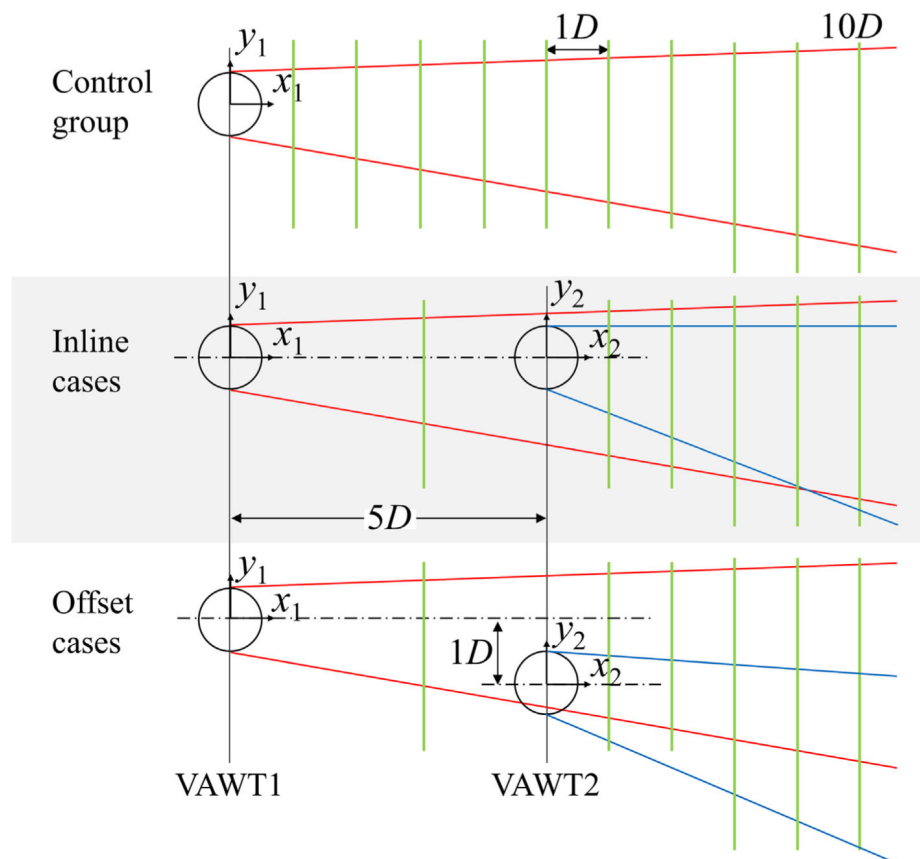
FIGURE 3   Schematic of the coordinate systems for the cases measured.

as the control group to evaluate the free wake in absence of the downwind turbine. The wake deflection mechanism of the isolated VAWTs and some velocity fields have already been presented in Huang et al[11] but are also shown here for the sake of completeness.

Six wake interaction cases with two turbines aligned along the streamwise direction and with 1D lateral offset are investigated. The blade pitch of the upwind VAWT, indicated with VAWT1, varies as aforementioned to yield different wake deflections; conversely, the downwind VAWT, indicated with VAWT2, operates at a constant zero pitch. The streamwise distance between the rotor centres is 5 rotor diameters (D). The VAWTs rotate at a speed of 800 rpm, resulting in a tip speed ratio (λ) of 2.5 relative to U_∞.

In addition, two coordinate systems are adopted: one has the origin at the rotor centre of VAWT1, the other at that of VAWT2. The selection of the coordinate systems is for the ease of discussion on the wake deflection relative to each VAWT. The relationship between the coordinates is given by the following equations:

$$x_1 = x_2 + 5D, y_1 = \begin{cases} y_2, \text{inline cases} \\ y_2 - 1D, \text{offset cases} \end{cases} \tag{1}$$

2.6 | Data acquisition and experiment procedures

For the control group, the PIV measurement planes range from 1D to 10D behind the VAWT; for the interaction cases, the PIV measurements are performed 2D upstream and 1D to 5D downstream of VAWT2. At each acquisition plane, 300 image pairs are taken at a frequency of 15 Hz to perform an ensemble average over a period of 20 s (266.7 rotations) (Table 1).

The time-averaged thrust forces of the control group are measured at free-stream velocities ranging from 3 to 7 ms^{-1}, corresponding to λ from 1.8 to 4.2. Curves of thrust coefficient versus λ are obtained (Figure 4). The thrusts ($C_{T,x}$ and $C_{T,y}$) are expressed as

TABLE 1 Description of the measured configurations.

|	Case	Description
Control group	P−10	Isolated VAWT with pitched blades, −10°
	P0	Isolated VAWT with zero pitch
	P10	Isolated VAWT with pitched blades, +10°
Inline group	P−10_0D ($\alpha_{p,1} = -10°, y_{\text{offset}}/D = 0$)	VAWT1 with −10° pitch, VAWT2 with zero transverse offset
	P0_0D ($\alpha_{p,1} = 0°, y_{\text{offset}}/D = 0$)	VAWT1 with zero pitch, VAWT2 with zero transverse offset
	P10_0D ($\alpha_{p,1} = 10°, y_{\text{offset}}/D = 0$)	VAWT1 with 10° pitch, VAWT2 with zero transverse offset
Offset group	P−10_1D ($\alpha_{p,1} = -10°, y_{\text{offset}}/D = 1$)	VAWT1 with −10° pitch, VAWT2 with 1 D transverse offset
	P0_1D ($\alpha_{p,1} = 0°, y_{\text{offset}}/D = 1$)	VAWT1 with zero pitch, VAWT2 with 1 D transverse offset
	P10_1D ($\alpha_{p,1} = 10°, y_{\text{offset}}/D = 1$)	VAWT1 with 10° pitch, VAWT2 with 1 D transverse offset
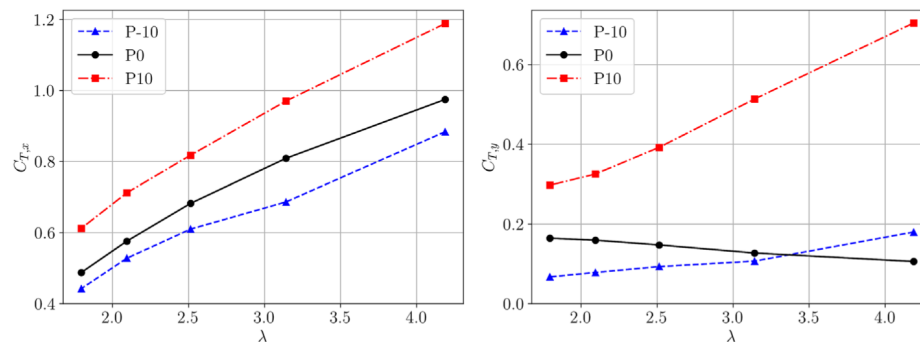
FIGURE 4 $C_{T,x}$-λ (left) and $C_{T,y}$-λ (right) curves of isolated P−10, P0, and P10.

$$C_T = \frac{T}{0.5\rho U_\infty^2 A},$$

(2)

where T is the streamwise or lateral force exerted on the flow, which is equal and opposite to the measured force applied to the VAWT. U_∞ is the free-stream velocity and A is the frontal area of the VAWT, 0.09 m^2.

3 | RESULTS AND DISCUSSION

3.1 | Wake dynamics of the control group

Because the presence of an upwind turbine affects the inflow conditions of downwind turbines, in this section, we assess the wake development of an isolated turbine (corresponding to the upwind turbine, VAWT1, in the interaction cases) with and without blade pitch.

3.1.1 | Force balance measurement results

The variation of the streamwise thrust coefficient ($C_{T,x}$) with the tip speed ratio λ in the control group is depicted in Figure 4 (left). With λ increasing, $C_{T,x}$ increases almost linearly. Similar trends within these tip speed ratios have been reported in the literature.[47,48] Take case P0 as the baseline; it is noticed that a positive pitch shifts the curve upwards, thus leading to a higher thrust coefficient at the same λ. Vice versa, a negative pitch shifts the curve downwards, resulting in a lower thrust coefficient at the same λ. The shifting of $C_{T,x}$ via blade pitching is consistent with that documented in Ferreira (2009),[49] where a VAWT with different pitch axes, rotating at a constant tip speed ratio, was simulated.
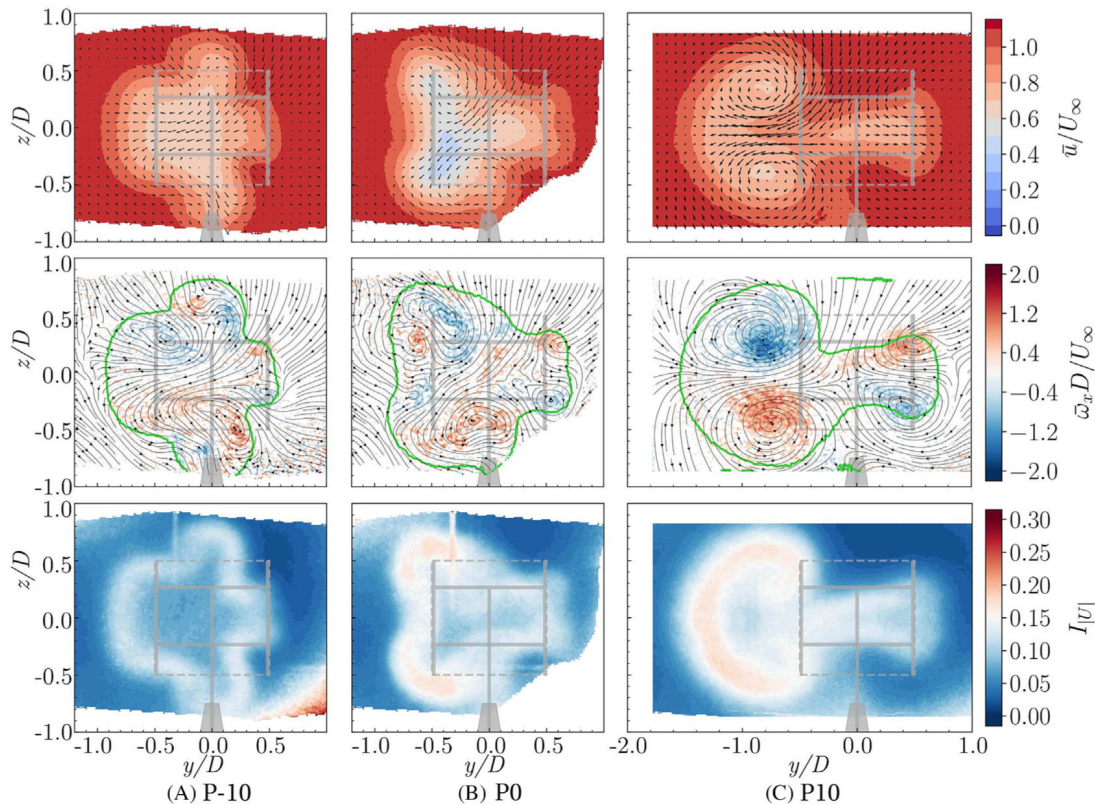

FIGURE 5 Contours of streamwise velocity with in-plane velocity vectors, vorticity with in-plane streamlines, and turbulence intensity for the isolated VAWT P−10, P0 and P10 at $x_1/D = 5$. Green contour lines indicate $u/U_\infty = 1$, showing the outline of the wake; grey schematics: the isolated VAWT.

The lateral force coefficient ($C_{T,y}$) - λ curves are presented in Figure 4 (right). P10 features much stronger lateral forces causing significant wake deflection as shown in Section 3.1.2; conversely, for the P0 and P$-$10 cases, $C_{T,y}$ remain below 0.2. The curves of P$-$10 and P10 cases feature monotonically increasing trends. However, the increase is much steeper for the P10 case. In contrast, the lateral force of P0 decreases slightly with increasing λ. The decrease of the lateral force is because as the rotation speed increases, the free-stream has less effect on the blade angle of attack (AoA) at advancing and retreating sides, and thus the AoA perceived at both sides are similar, such that lateral forces are cancelled out at high λ. Similar trends have been reported in Huang et al,[46] where the forces of the same VAWT rotor were measured with a different balance system. On the contrary, for P$-$10 and P10, the rotor has higher lateral force at high λ. This is due to the fact that the blades in advancing side operates in exceedingly high AoA at lower λ and suffers from deep dynamic stall. As λ increases, the AoA decreases and the stall effects attenuate. Hence, the blades produce higher lift and thus more lateral forces.

TABLE 2 Measured forces of the isolated pitched turbines or downwind turbines with zero pitch, with available momentum ($< U_0^2/U_\infty^2 >$) and available power ($< U_0^3/U_\infty^3 >$) calculated from the velocity field of the isolated pitched turbines at $5D$ downstream the rotor. Shaded cells: inline cases; red numbers: increment compared to P0_0D.

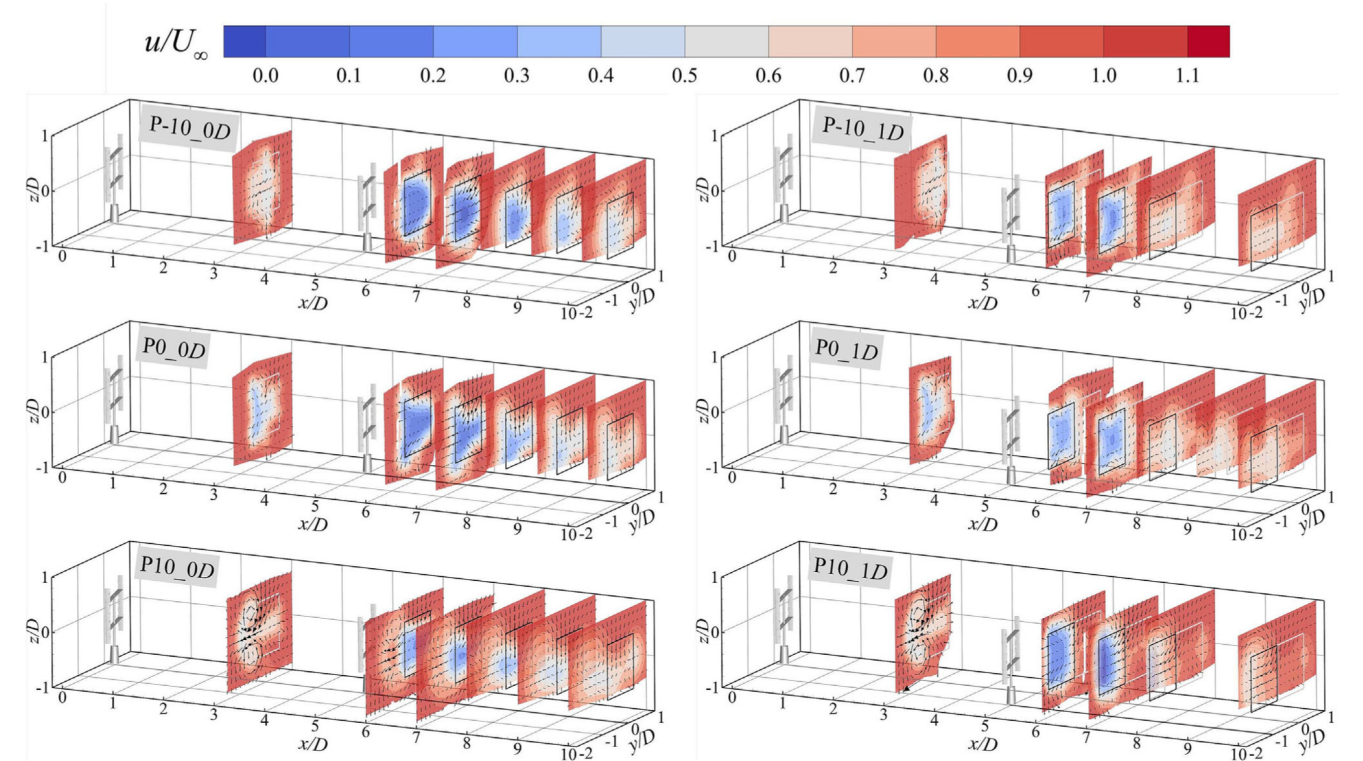|	Case	AM $\equiv < U_0^2/U_\infty^2 >$ [-]	AP$\equiv < U_0^3/U_\infty^3 >$ [-]	T_x [N]	T_y [N]
Isolated turbines	P$-$10	1	1	0.80	0.12
	P0	1	1	0.88	0.19
	P10	1	1	1.09	0.52
Downwind turbines	P$-$10_0D ($\alpha_{p,1} = -10°$, $y_{offset}/D = 0$)	0.62 (+9.7%)	0.50 (+13.6%)	0.64 (+4.9%)	0.12
	P0_0D ($\alpha_{p,1} = 0°$, $y_{offset}/D = 0$)	0.56	0.44	0.61	0.14
	P10_0D ($\alpha_{p,1} = 10°$, $y_{offset}/D = 0$)	0.81 (+44.6%)	0.74 (+68.2%)	0.69 (+13.1%)	0.12
	P$-$10_1D ($\alpha_{p,1} = -10°$, $y_{offset}/D = 1$)	0.85 (+51.8%)	0.82 (+86.4%)	—	—
	P0_1D ($\alpha_{p,1} = 0°$, $y_{offset}/D = 1$)	0.83 (+48.2%)	0.80 (+81.8%)	0.73 (+19.7%)	0.14
	P10_1D ($\alpha_{p,1} = 10°$, $y_{offset}/D = 1$)	0.62 (+10.7%)	0.50 (+13.6%)	—	—

FIGURE 6 Overview of the placement of the turbine and measured streamwise velocity contours. Grey squares denote the frontal area of the upwind turbine (VAWT1) while black squares for the downwind turbine (VAWT2).

3.1.2 | PIV measurement results

To evaluate the impact of the upwind turbines on the inflow of the downwind ones, the velocity, vorticity and turbulence fields in the wake of isolated VAWTs with different pitch angles are measured with PIV and illustrated in Figure 5. Data at $x_1/D = 5$ is selected in accordance with the locations of downwind VAWTs' rotor centre. Data at different downwind locations have been published in the previous article[50] and are presented in Appendix A of the present work for the sake of completeness.
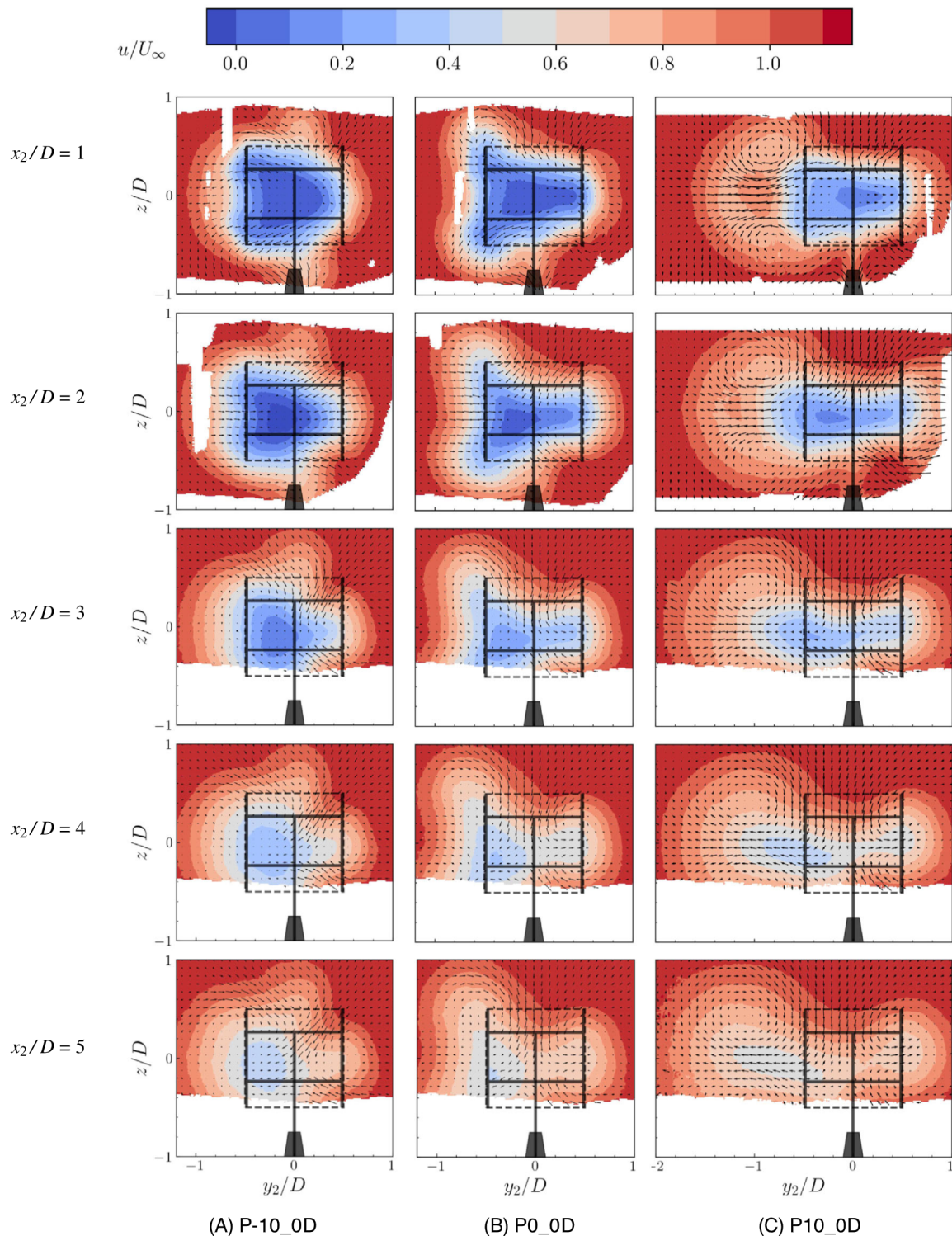
FIGURE 7 Streamwise velocity contours with in-plane vectors for inline cases, at the near wake of the downwind turbine (VAWT2) ($x_2/D = 1, 2, 3, 4, 5$). Black schematics represent VAWT2.

All the contours are almost symmetric with respect to $z/D = 0$, because of the absence of the ground, except for the region in proximity to the wake of the tower. P−10 features the minimum lateral wake deflection among the three cases. There is elongation along the span-wise direction around the centre of the wake. The wake of P0 features a trapezoidal shape with concave sidelines, and is slightly deflected towards negative y. In contrast, the wake of P10 has a significant deflection to the left, and a faster velocity recovery around $y/D = 0$. The streamwise vorticity fields, illustrated in the second line of Figure 5, are characterised by a set of counter-rotating vortex pairs (CVPs).[9,13,46] The wakes of P−10 and P0 feature more than two pairs of counter-rotating vortices, whereas in the wake of P10 only two strong CVPs are present. The turbulence intensity contours, depicted in the third line of Figure 5, clearly show that the highest turbulence intensity is concentrated along the perimeters of the wakes.

The isolated VAWTs with different blade-pitch angles feature different cross-flow thrusts, and thus produce different wake deflections. The relation between the rotor loading and the wake deflection has been reported in ref-,[11] while the amount of deflection is discussed with a wake centre technique in Section 3.2.3. Additionally, the variation in blade pitches results in completely different structures of streamwise vorticity, as well as different levels of turbulence intensity (TI), and hence, different wake recovery rates. In particular, the case P10 (with positive 10° pitch) manifests the strongest counter-rotating vortex pair and the highest TI level, resulting in the fastest wake recovery even though its initial momentum deficit is the highest.
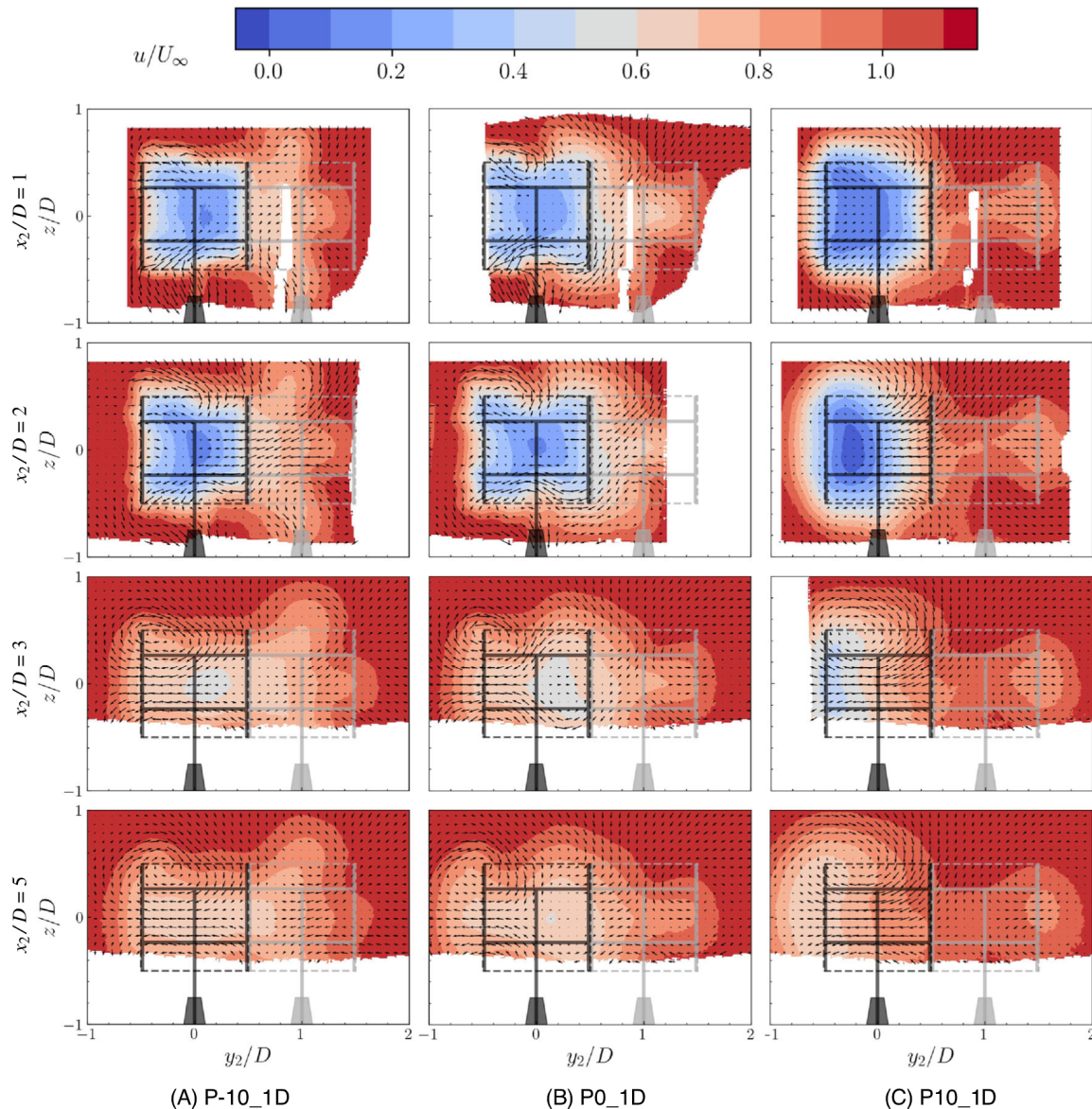

FIGURE 8 Streamwise velocity contours with in-plane vectors for offset cases, at the near wake of the downwind VAWT (VAWT2) ($x_2/D = 1, 2, 3, 5$). Grey and Black schematics represent VAWT1 and VAWT2, respectively.

3.2 | Wake interactions with the presence of the downwind turbines

3.2.1 | Rotor loading

The measured forces T_x and T_y of the downwind VAWT are listed in Table 2. The estimation of available power (AP$\equiv$ < U_0^3/U_∞^3 >) introduced in the previous work[11] for a hypothetical downwind turbine is adopted here to discuss the wake effect on the performance of the downwind rotor (VAWT2). U_0 is the hypothesised inflow velocity. For VAWT1 it equals to the freestream velocity U_∞; whereas for VAWT2, it is the streamwise velocity in the wake of the isolated VAWTs at $x_1/D = 5$. It is assumed that the VAWT2's effect on the inflow can be omitted, and the cross-flow velocities in the wake of isolated VAWTs are negligible compared to the streamwise velocity. The angle bracket denotes a spatial average within the frontal area of VAWT2, which is a square region located aligned with the upwind turbine (VAWT1) or with 1D offset, at $x_1/D = 5$. Available momentum (AM$\equiv$ < U_0^2/U_∞^2 >) estimations are also listed in Table 2.

Taking the case where $\alpha_{p,1} = -10°$, $y_{\text{offset}}/D = 0$ (P0_0D) as the baseline, for the inline cases, when the upwind turbine has 10° pitch, the AM increases the most (+44.6%). This is due to the wake deflection and faster wake recovery produced by the upwind VAWT. The AP follows the same trend of the AM. In contrast, when the downwind VAWT (VAWT2) is translated 1D laterally, the inflow momentum in cases P−10_1D and P0_1D increases remarkably (+51.8% and +48.2%), while it increases slightly in P10_1D (+10.7%). This is due to the largely deflected wake towards the VAWT2 in the latter case. Moreover, P−10_1D features a higher AM increment than P0_1D, because P−10's wake is deflected slightly away from VAWT2 compared to that of P0. The wake deflection can be appreciated in Section 3.2.2.

The measured streamwise thrusts confirm that the estimation of AM and AP in the wake of isolated VAWT is in accordance with the performance of the downwind turbine. P0_0D features the least AM and AP and thus T_x of VAWT2 in this case is the minimum among all the cases. P10_0D has the highest AM and AP among the inline cases, proving that the wake deflection due to a positive pitch can be beneficial to the downwind wind turbines. The AM and AP in the 1D offset cases show that translating the VAWT2 away from the wake centre of VAWT1 will mitigate the wake effect and gain more power for downwind turbines. The wake centre is discussed in Section 3.2.3.

3.2.2 | Velocity fields

An overview of the placement of the VAWTs and corresponding measurement planes is given in Figure 6, where the centre of the upwind VAWT (VAWT1) is selected as the origin of the global coordinate system. The velocity contour 2D ahead of the downwind turbine (VAWT2) is highly similar to that measured in the isolated turbine cases at the same location (3D behind VAWT1; see Appendix A). This confirms the assumption made in Section 3.2.1 that the VAWT2's effect on the inflow is negligible.

Figure 7 illustrates comparisons of the streamwise velocity contours behind VAWT2, where the origin of the coordinate system is the centre of VAWT2. The black outline of VAWT1 denotes its frontal area and the transverse location, which is the same as that of VAWT1 in this case. For all the three inline cases, the wake of VAWT2 is embedded into the background wake of VAWT1, and thus the wake deformation is significantly affected by the inflow velocity field.

Compared to the control group (see also Appendix A), the wakes of the inline cases remain similar to that of the isolated VAWTs, but the velocity deficits in the wake centre are increased due to the presence of the downwind VAWT. P−10_0D features a deeper velocity deficit than
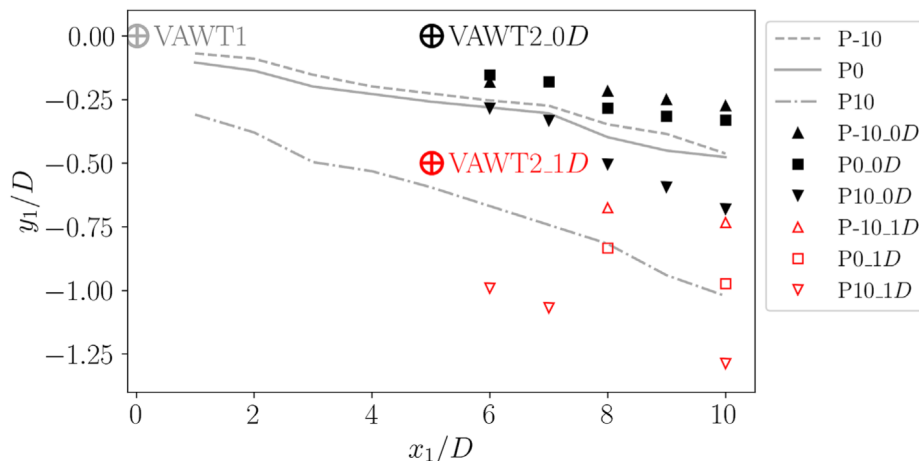

FIGURE 9 Wake centre development of all the cases. ⊕ denotes the rotor centre. Missing points for the 1D offset cases due to two reasons: a) measurement planes at $x_1/D = 9$ are not available for these cases; b) unrealistic estimations due to object reflection in the PIV measurements.

P0_0*D*, because the former exerts a higher thrust against the free-stream while the lateral forces of the two are similar. In contrast, P10_0*D* exerts the highest T_x and T_y, but the lowest velocity deficit. This is due to two reasons: First, a large portion of the extracted streamwise momentum is transferred to the horizontal deflection, and that explains the largest wake deflection compared with the other two cases; second, its significant wake deformation yields a faster recovery, by enhancing the entrainment of momentum via the advection and the increased wake-free-stream interface.[11]
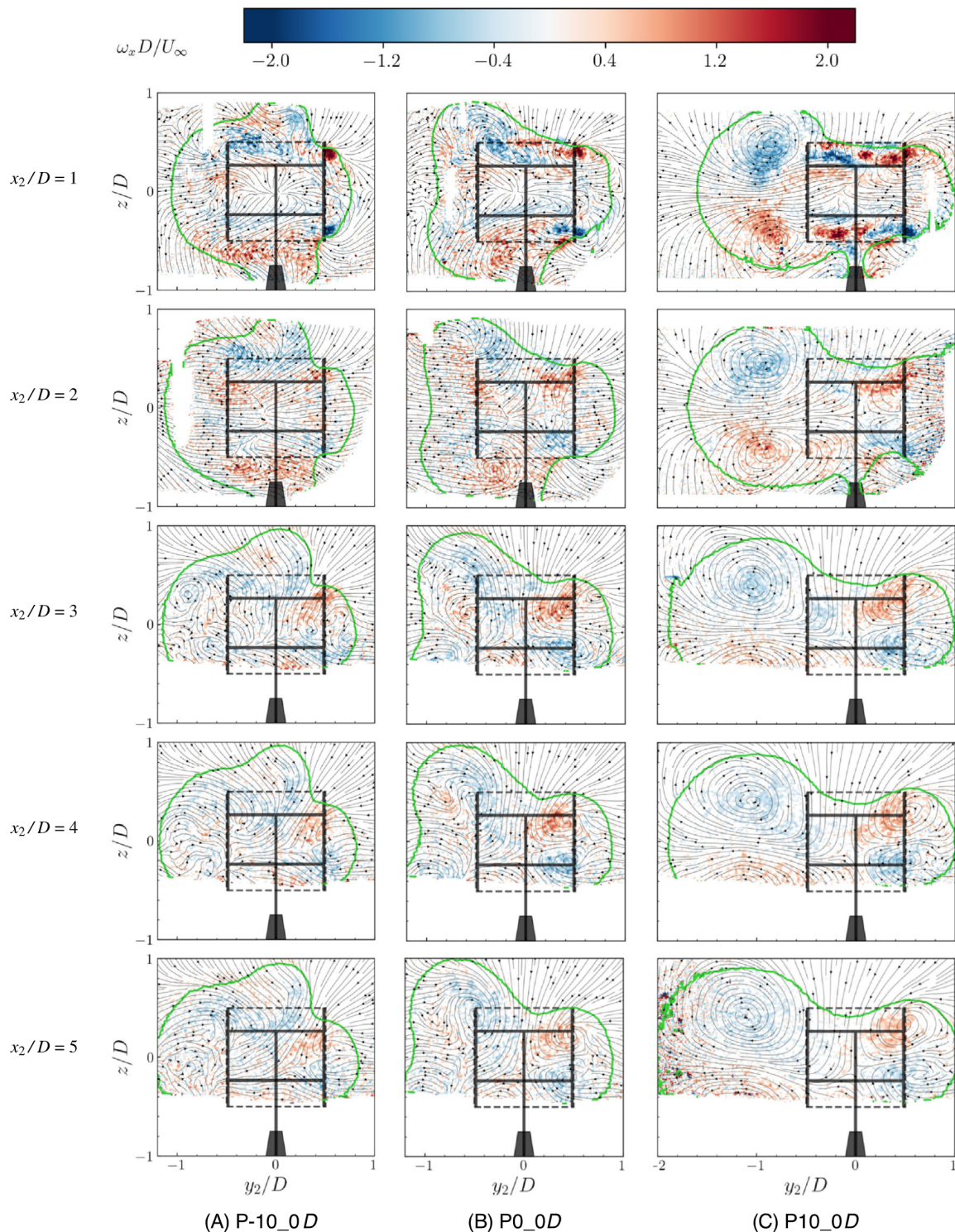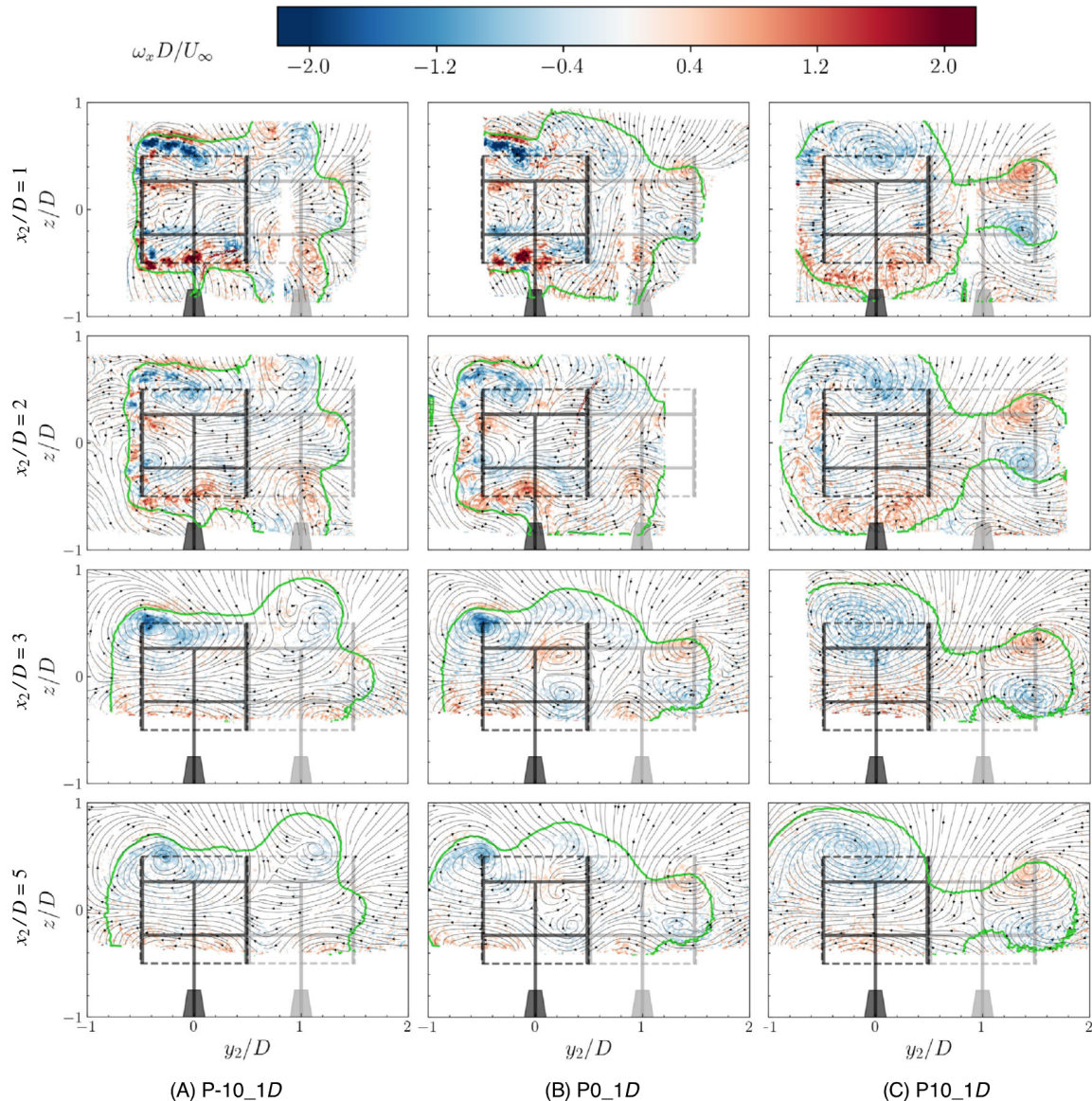

FIGURE 10 Streamwise vorticity contours with in-plane streamlines for inline cases, at the near wake of the downwind VAWT (VAWT2) ($x_2/D = 1, 2, 3, 4, 5$). Green contour lines indicate $u/U_\infty = 1$. Black schematics represent VAWT2.

The velocity fields in the wake of the offset cases are illustrated in Figure 8. The black outline represents the downwind VAWT2 while the grey outline is for the upwind VAWT1. The origin of the coordinate system in the graphics is the centre of VAWT2. In the near wake region ($x_2/D = 1$), the outlines of the wakes of VAWT2 are similar among the three different configurations. The wake interaction in P−10_1D and P0_1D occurs at regions where the right edge of VAWT2's wake overlapped with the left of VAWT1's wake; whereas in P10_1D, the wake of VAWT2 is bounded by the wake of VAWT1 entirely. The wakes of P−10_1D and P0_1D look like the superposition of two isolated wakes, where the right and the left parts are the wakes of VAWTs with and without pitched blades, respectively. However, the wake outline of P10_1D is similar to the wake of isolated P10, except for a deeper velocity deficit.

3.2.3 | Wake centre

The wake centre is calculated by evaluating the centre of mass of the velocity deficit[15,51]:

$$y_c(x) = \frac{\iint y \Delta u(x,y,z)\, dydz}{\iint \Delta u(x,y,z)\, dydz},$$ (3)

FIGURE 11 Streamwise vorticity contours with in-plane streamlines for offset cases, at the near wake of the downwind VAWT (VAWT2) ($x_2/D = 1,2,3,5$). Green contour lines indicate $u/U_\infty = 1$. Grey and black schematics represent VAWT1 and VAWT2, respectively.

where $\Delta u(x,y,z) = U_\infty - u(x,y,z)$. The integrals are computed over cross-sectional planes, perpendicular to the streamwise velocity. The coordinate system is based on the isolated VAWT. Only the lateral (horizontal) coordinate of the wake centre is discussed in this article for the sake of simplicity.

As shown in Figure 9, for the control group (grey), the 10° positive blade-pitch of the isolated VAWT more than doubles the wake deflection, while the negative pitch slightly decreases the deflection. For the inline cases (black), the VAWT2's wake deflection features a similar trend as the
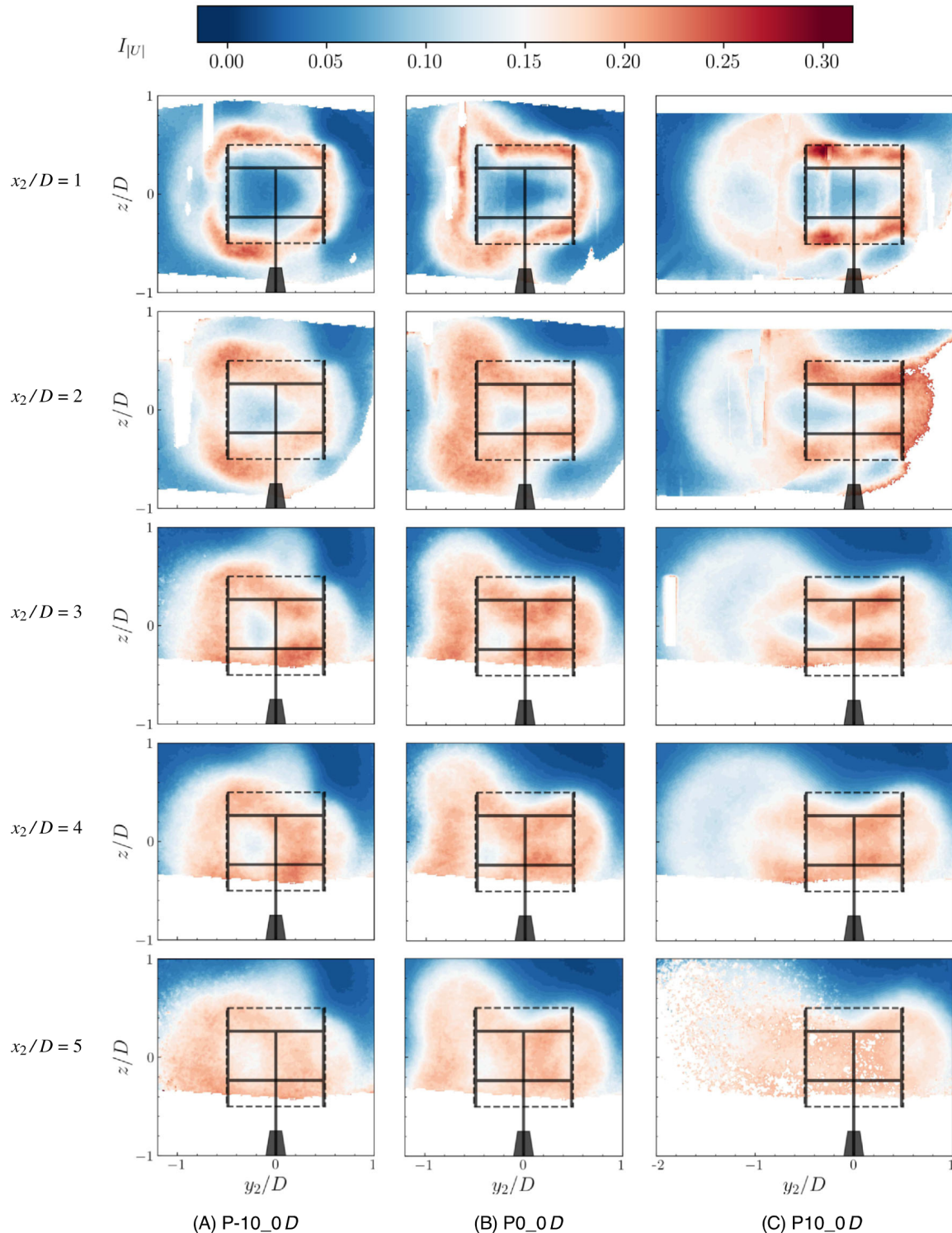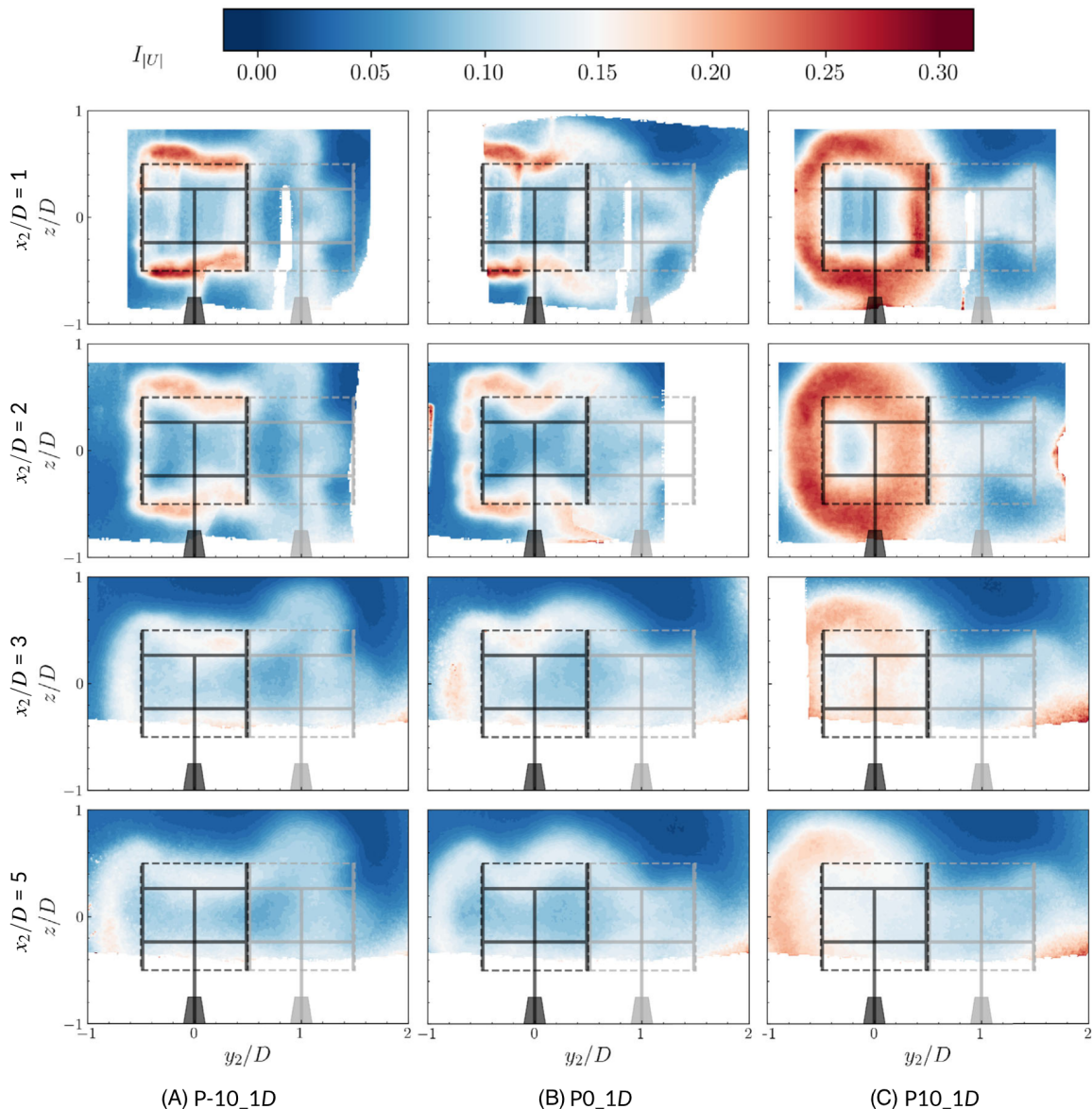

FIGURE 12 Contours of turbulence intensity magnitude for inline cases, at the near wake of the downwind VAWT (VAWT2) ($x_2/D = 1, 2, 3, 4, 5$). Black schematics represent VAWT2.

isolated turbine, with positively pitched VAWT1 increasing the deflection, and vice versa. In contrast, when the VAWT2 is translated horizontally (0D cases vs. 1D cases), the wake centres are translated significantly.

3.2.4 | Streamwise vorticity

The streamwise vorticity of the inline and 1D-offset cases are shown in Figures 10 and 11, respectively. For the inline cases P−10_0D, P0_0D and P10_0D, the vortex generated by VAWT2 interacts directly with that generated by VAWT1. They are eventually merged together and keep the same macroscopic behaviour as that of the corresponding isolated VAWT. In the wake of P10_0D, the vorticity of VAWT2 is not interacting with the CVPs of P10 initially at $x_2/D = 1$, because their locations are relatively far apart. However, the CVPs of P10 are strong enough to merge with those of the VAWT2 as the wake develops further downstream.

A similar phenomenon occurs when the downwind VAWT2 is translated out of the centre of the upwind VAWT1's wake, such that its vorticity does not directly interact with that of VAWT1, and thus a double-layer structure[11] remains at its near wake ($x_2/D = 1$, P−10_1D and P0_1D). However, in these two cases, the background vorticity is not strong enough to merge the vorticity of VAWT2, resulting in a structure with spread

FIGURE 13 Contours of turbulence intensity magnitude for offset cases, at the near wake of the downwind VAWT (VAWT2) ($x_2/D = 1, 2, 3, 5$). Grey and black schematics represent VAWT1 and VAWT2, respectively.

multi-CVPs. On the contrary, in the wake of P10_1D, the vorticity of VAWT2 interacts directly with the strongest counter-rotating vortex pair of VAWT1, and is completely merged with it at $x_2/D = 5$. This leads to an almost unchanged wake outline compared to that of P10.

3.2.5 | Turbulence intensity

The measured turbulence intensity magnitudes are presented in Figure A5 (isolated turbines) and Figures 12 and 13 (wakes interactions). The turbulence intensity in the control group depicts the footprint of the wake, with the turbulence concentrating along the wake perimeter, that is, the wake-freestream interface.

The presence of the downwind VAWT increases the turbulence in the wake. In Figure 12, the increased turbulence intensity initially distributes along the wake outline of VAWT2 at $x_2/D = 1$, as in a simple overlap with the background turbulence. Merging of the turbulence occurs vigorously, and the turbulence intensity is smeared almost uniformly within the wake region at $x_2/D = 5$.

When the wake of VAWT2 is shifted out of the wake centre of VAWT1, the turbulence interaction becomes less vigorous, as illustrated in Figure 13. That is because the counter-rotating vortex pairs are shifted away from each other, as discussed in Section 3.2.4. For example, in cases P−10_1D and P0_1D, the turbulence is increased at $-0.5 < y_2/D < 0.5$, concentrating on the wake perimeter of VAWT2. At $x_2/D = 3$ and 5, a merged wake and a new outline are generated, and thus, the turbulence is distributed along the new edges. On the contrary, in P10_1D, the turbulence intensity around VAWT2 increases dramatically since $x_2/D = 1$, due to a direct interaction of the CVPs. As reported in the literature,[7,52] higher TI is beneficial to faster wake recovery. The turbulence fields presented in the section indicate an acceleration of the wake recovery via enhancing the TI.

3.2.6 | Available power behind VAWT2

The normalised available power distribution behind the downwind VAWT (VAWT2) at $x_2/D = 3$ and 5 is depicted in Figure 14, columns 2 and 3. The procedure for the AP calculation has been briefly introduced in Section 1, and more details can be found in Huang et al.[11] In Figure 14, the AP of isolated VAWTs is presented in the first column for comparison, showing the available power when no downwind turbine is implemented. $x_2/D = 3$ and 5 corresponds to $x_1/D = 8$ and 10 in the coordinate system of isolated VAWTs. In the second and third columns, the vertical axis denotes the averaged wind power within the frontal area of a hypothetical VAWT (a third VAWT, VAWT3) placed downwind of VAWT2, the lateral location of its rotor centre is presented relative to the upwind VAWT (VAWT1), that is, y_1/D, for the sake of clarity.

Generally, one would extract more wind energy by placing the VAWT3 out of the valley of AP curves. Inline cases P−10_0D and P0_0D, offset case P10_1D exhibit narrower distributions of low AP than the others, because VAWT2 mainly operates in the wake of VAWT1 in these cases. The narrower distribution means more abundant AP along transverse locations for the hypothetical VAWT. Among the three cases, P10_1D has the narrowest AP distribution, showing the efficacy of wake deflection.
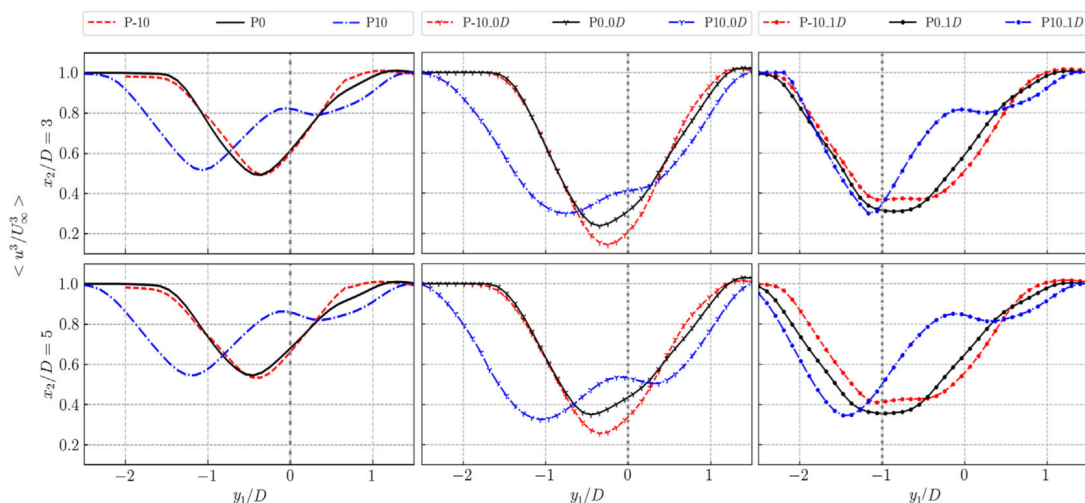

FIGURE 14 Available power distribution along transverse locations (y_1/D) at $x_2/D = 3$ and 5, corresponding to $x_1 = 8$ and 10 for the control group. For two turbine cases, grey dotted lines denote the rotor centre of the downwind VAWT (VAWT2).

However, in these three cases, VAWT2 has to extract energy in a decelerated and highly turbulent inflow; The wake effect as such will reduce its power extraction. Therefore, VAWT2 are moved out of VAWT1's wake in the other cases, that is, offset cases P−10_1*D* and P0_1*D*, and the inline case P10_0*D*. The AP curves feature wider valleys for these cases, indicating more wind power extracted by VAWT1 and VAWT2 than in cases where the upwind turbine's wake entirely bounds the downwind turbine. The trade-off is, however, the reduced high AP region for VAWT3.

4 | CONCLUSIONS

The wake interaction of two VAWTs placed upwind and downwind has been investigated experimentally via PIV and load measurements. The distance between the two turbines in the flow direction is 5*D*, and flow measurements cover a region 10*D* downwind of the first turbine (5*D* downwind of the second turbine).

The VAWT blade pitching is effective in modifying the rotor loading and deflecting the wake. With a positive 10° pitch, the VAWT increases the lateral force and deflects the wake centre more than twice compared to the zero-pitch case. The deflected wake changes the inflow condition of the downwind VAWT inline with the upwind turbine (an increment of 44.6% available momentum at 5*D* downstream the rotor than P0), and thus increases the overall extraction of streamwise momentum ($C_{T,x}$ of VAWT2 increased 13.1%).

The study also covers in detail the case in which the wake is deflected towards the second turbine, to explore the more complex and undesirable situation. The wake of the upwind VAWT has a dominant effect on the wake topology and recovery of the downwind VAWT, provided that the latter is fully immersed by the wake of the upwind one. The vorticity system plays an important role in the interaction. When the counter-rotating vortices generated by the VAWTs are placed close enough, they lead to vigorous interaction and merging, thus increasing the turbulence intensity and in turn the wake recovery rate. On the contrary, if they are placed far enough but not separated completely, the merging of the wakes' shear layers takes the lead while the counter-rotating vortices are more effective in deforming the wake instead of increasing turbulence.

Deflecting the upwind turbine's wake and shifting the downwind rotor can both mitigate the wake effect, although wake deflection via blade pitch is apparently more flexible and easier to control in an array configuration. The wake deflection and the modified streamwise vortical system retain till the far wake, deflecting the downwind turbine's wake and enhancing the momentum recovery.

The results demonstrate the potential of VAWTs for enhanced wake recovery and provide a database for model validation. Additionally, they raise questions for future research on the maximum potential of energy recovery and how it can be achieved.

CONFLICT OF INTEREST STATEMENT

The authors report no conflict of interest.

PEER REVIEW

The peer review history for this article is available at https://www.webofscience.com/api/gateway/wos/peer-review/10.1002/we.2863.

DATA AVAILABILITY STATEMENT

The data that support the findings of this study are openly available in 4TU ResearchData at https://doi.org/10.4121/17802134.

ORCID

Ming Huang https://orcid.org/0000-0003-3942-3871

REFERENCES

1. Fleming, P, Annoni, J, Shah, JJ, et al. Field test of wake steering at an offshore wind farm. *Wind Energ Sci*. 2017;2:229-239. doi:10.5194/wes-2-229-2017
2. Fleming, P, King, J, Dykes, K, et al. Initial results from a field campaign of wake steering applied at a commercial wind farm—part 1. *Wind Energy Sci*. 2019;4(2):273-285. doi:10.5194/WES-4-273-2019
3. Meyers, J, Meneveau, C. Optimal turbine spacing in fully developed wind farm boundary layers. *Wind Energy*. 2012;15(2):305-317. doi:10.1002/WE.469
4. Stevens, RJ. Dependence of optimal wind turbine spacing on wind farm length. *Wind Energy*. 2016;19(4):651-663. doi:10.1002/we.1857
5. Stevens, RJ, Hobbs, BF, Ramos, A, Meneveau, C. Combining economic and fluid dynamic models to determine the optimal spacing in very large wind farms. *Wind Energy*. 2017;20(3):465-477. doi:10.1002/we.2016

6. Stevens, RJAM, Gayme, DF, Meneveau, C. Effects of turbine spacing on the power output of extended wind-farms. *Wind Energy*. 2016;19(January): 359-370. doi:10.1002/we

7. Chatelain, P, Duponcheel, M, Zeoli, S, Buffin, S, Caprace, DG, Winckelmans, G, Bricteux, L. Investigation of the effect of inflow turbulence on vertical axis wind turbine wakes. *Wake Conference 2017*: IOP Publishing; 2017:12011.

8. Dabiri, JO. Potential order-of-magnitude enhancement of wind farm power density via counter-rotating vertical-axis wind turbine arrays. *J Renew Sustain Energy*. 2011;3(4):43104. doi:10.1063/1.3608170

9. Rolin, VFC, Porté-Agel, F. Experimental investigation of vertical-axis wind-turbine wakes in boundary layer flow. *Renew Energy*. 2018;118:1-13. doi:10.1016/j.renene.2017.10.105

10. Boudreau, M, Dumas, G. Comparison of the wake recovery of the axial-flow and cross-flow turbine concepts. *J Wind Eng Indust Aerodyn*. 2017;165-(March):137-152. doi:10.1016/j.jweia.2017.03.010

11. Huang, M, Sciacchitano, A, Ferreira, C. On the wake deflection of vertical axis wind turbines by pitched blades. *Wind Energy*. 2023;26(4):365-387.

12. Tescione, G, Ragni, D, He, C, Ferreira, CJ, van Bussel, GJW. Near wake flow analysis of a vertical axis wind turbine by stereoscopic particle image velocimetry. *Renew Energy*. 2014;70:47-61. doi:10.1016/j.renene.2014.02.042

13. Ryan, KJ, Coletti, F, Elkins, CJ, Dabiri, JO, Eaton, JK. Three-dimensional flow field around and downstream of a subscale model rotating vertical axis wind turbine. *Experiments in Fluids*. 2016;57(3):38. doi:10.1007/s00348-016-2122-z

14. Araya, DB, Colonius, T, Dabiri, JO. Transition to bluff-body dynamics in the wake of vertical-axis wind turbines. *J Fluid Mech*. 2017;813:346-381. doi:10.1017/jfm.2016.862

15. Wei, NJ, Brownstein, ID, Cardona, JL, Howland, MF, Dabiri, JO. Near-wake structure of full-scale vertical-axis wind turbines. *J Fluid Mech*. 2021;914: 17. doi:10.1017/jfm.2020.578

16. Bachant, P, Wosnik, M. Characterising the near-wake of a cross-flow turbine. *J Turbul*. 2015;16(4):392-410. doi:10.1080/14685248.2014.1001852

17. Ouro, P, Runge, S, Luo, Q, Stoesser, T. Three-dimensionality of the wake recovery behind a vertical axis turbine. *Renew Energy*. 2019;133:1066-1077. doi:10.1016/j.renene.2018.10.111

18. Mendoza, V, Bachant, P, Ferreira, C, Goude, A. Near-wake flow simulation of a vertical axis turbine using an actuator line model. *Wind Energy*. 2019; 22(2):171-188. doi:10.1002/we.2277

19. Kinzel, M, Mulligan, Q, Dabiri, JO. Energy exchange in an array of vertical-axis wind turbines. *J Turbul*. 2013;14(6):38-39. doi:10.1080/14685248.2013.825725

20. Ahmadi-Baloutaki, M, Carriveau, R, Ting, DS-K. A wind tunnel study on the aerodynamic interaction of vertical axis wind turbines in array configurations. *Renew Energy*. 2016;96:904-913. doi:10.1016/j.renene.2016.05.060

21. Lam, HF, Peng, HY. Measurements of the wake characteristics of co- and counter-rotating twin H-rotor vertical axis wind turbines. *Energy*. 2017;131: 13-26. doi:10.1016/j.energy.2017.05.015

22. Brownstein, ID, Wei, NJ, Dabiri, JO. Aerodynamically interacting vertical-axis wind turbines: performance enhancement and three-dimensional flow. *Energies*. 2019;12(14):2724. doi:10.3390/en12142724

23. Mereu, R, Federici, D, Ferrari, G, Schito, P, Inzoli, F. Parametric numerical study of Savonius wind turbine interaction in a linear array. *Renew Energy*. 2017;113:1320-1332. doi:10.1016/j.renene.2017.06.094

24. Posa, A. Wake characterization of coupled configurations of vertical axis wind turbines using Large Eddy Simulation. *Int J Heat Fluid Flow*. 2019;75:27-43. doi:10.1016/j.ijheatfluidflow.2018.11.008

25. Sahebzadeh, S, Rezaeiha, A, Montazeri, H. Impact of relative spacing of two adjacent vertical axis wind turbines on their aerodynamics. *Journal of physics: Conference series*: IOP Publishing; 2020:42002.

26. Hezaveh, SH, Bou-Zeid, E. Mean kinetic energy replenishment mechanisms in vertical-axis wind turbine farms. *Phys Rev Fluids*. 2018;3(9):94606. doi:10.1103/PhysRevFluids.3.094606

27. Mendoza, V, Goude, A. Improving farm efficiency of interacting vertical-axis wind turbines through wake deflection using pitched struts. *Wind Energy*. 2019;22(4):538-546. doi:10.1002/we.2305

28. Silva, JE, Danao, LAM. Individual rotor and overall cluster performance. *Energies*. 2021;14:1-22. doi:10.3390/en14061567

29. Kinzel, M, Araya, DB, Dabiri, JO. Turbulence in vertical axis wind turbine canopies. *Phys Fluids*. 2015;27:115102. doi:10.1063/1.4935111

30. Craig, AE, Dabiri, JO, Koseff, JR. A kinematic description of the key flow characteristics in an array of finite-height rotating cylinders. *J Fluids Eng*. 2016;138(7):70906. doi:10.1115/1.4032600

31. Craig, AE, Dabiri, JO, Koseff, JR. Flow kinematics in variable-height rotating cylinder arrays. *J Fluids Eng*. 2016;138(11):111203. doi:10.1115/1.4033676

32. Jensen, NO. A note on wind generator interaction. *Risø National Laboratory*. Roskilde: Risø National Laboratory; 1983.

33. Frandsen, S, Barthelmie, R, Pryor, S, Rathmann, O, Larsen, S, Højstrup, J, Thøgersen, M. Analytical modelling of wind speed deficit in large offshore wind farms. *Wind Energy*. 2006;9(1-2):39-53. doi:10.1002/we.189

34. Larsen, GC. *A Simple Wake Calculation Procedure*, Vol. 2760: Risø National Laboratory; 1988.

35. Stevens, RJAM, Meneveau, C. Flow structure and turbulence in wind farms. *Ann Rev Fluid Mech*. 2017;49:311-339. doi:10.1146/annurev-fluid-010816-060206

36. Porté-Agel, F, Bastankhah, M, Shamsoddin, S. Wind-turbine and wind-farm flows: a review. *Bound-Layer Meteorol*. 2020;174(1):1-59.

37. Zong, H, Porté-Agel, F. A momentum-conserving wake superposition method for wind farm power prediction. *J Fluid Mech*. 2020;889:A8. doi:10.1017/jfm.2020.77

38. Scott, R, Viggiano, B, Dib, T, Ali, N, Hölling, M, Peinke, J, Cal, RB. Wind turbine partial wake merging description and quantification. *Wind Energy*. 2020;23(7):1610-1618. doi:10.1002/we.2504

39. Pierella, F, Krogstad, PerAAge, Sætran, L. Blind Test 2 calculations for two in-line model wind turbines where the downstream turbine operates at various rotational speeds. *Renew Energy*. 2014;70:62-77. doi:10.1016/j.renene.2014.03.034

40. Sun, H, Gao, X, Yang, H. A review of full-scale wind-field measurements of the wind-turbine wake effect and a measurement of the wake-interaction effect. *Renew Sustain Energy Rev*. 2020;132(2019):110042. doi:10.1016/j.rser.2020.110042

41. Vogel, CR, Willden, RHJ. Investigation of wind turbine wake superposition models using Reynolds-averaged Navier-Stokes simulations. *Wind Energy*. 2020;23(3):593-607. doi:10.1002/we.2444

42. Ennis, BL, Griffith, DT. System Levelized Cost of Energy Analysis for Floating Offshore Vertical-Axis Wind Turbines, Albuquerque, New Mexico 87185 and Livermore, California 94550, Sandia National Laboratories; 2018.

43. Paulsen, US, Borg, M, Madsen, HA, et al. Outcomes of the DeepWind conceptual design. *Energy Procedia*. 2015;80:329-341. doi:10.1016/j.egypro.2015.11.437

44. Lignarolo, LEMM, Ragni, D, Krishnaswami, C, et al. Experimental analysis of the wake of a horizontal-axis wind-turbine model. *Renew Energy*. 2014;70: 31-46. doi:10.1016/j.renene.2014.01.020

45. Lignarolo, LE, Ragni, D, Scarano, F, Simão Ferreira, CJ, Van Bussel, GJW. Tip-vortex instability and turbulent mixing in wind-turbine wakes. *J Fluid Mech*. 2015;781:467-493. doi:10.1017/jfm.2015.470

46. Huang, M, Ferreira, C, Sciacchitano, A, Scarano, F. Experimental comparison of the wake of a vertical axis wind turbine and planar actuator surfaces. *J Phys Conf Ser*. 2020;1618(5):52063. doi:10.1088/1742-6596/1618/5/052063

47. Rezaeiha, A, Montazeri, H, Blocken, B. Characterization of aerodynamic performance of vertical axis wind turbines: impact of operational parameters. *Energy Convers Manag*. 2018;169:45-77. doi:10.1016/j.enconman.2018.05.042

48. Rezaeiha, A, Montazeri, H, Blocken, B. Towards optimal aerodynamic design of vertical axis wind turbines: impact of solidity and number of blades. *Energy*. 2018;165:1129-1148. doi:10.1016/j.energy.2018.09.192

49. Ferreira, CS. The near wake of the VAWT 2D and 3D views of the VAWT aerodynamics. *doctoral thesis*. Delft, Netherlands; 2009.

50. Huang, M, Ferreira, C, Sciacchitano, A, Scarano, F. Wake scaling of actuator discs in different aspect ratios. *Renew Energy*. 2022;183:866-876. doi:10.1016/j.renene.2021.11.045

51. Howland, MF, Bossuyt, J, Martínez-Tossas, LA, Meyers, J, Meneveau, C. Wake structure in actuator disk models of wind turbines in yaw under uniform inflow conditions. *J Renew Sustain Energy*. 2016;8:43301.

52. Gambuzza, S, Ganapathisubramani, B. The influence of freestream turbulence on the development of a wind turbine wake. *J Fluid Mech*. 2023; 963(A19):1-37. doi:10.1017/jfm.2023.302

APPENDIX A: WAKE OF THE ISOLATED VAWT WITH DIFFERENT FIXED BLADE PITCHES

A.1 | Velocity fields

The time-averaged streamwise velocity contours and in-plane velocity vectors of the isolated VAWT with different pitch angles are presented in Figures A1 and A2. The velocity contours at $x_1/D = 6, 8, 10$ are illustrated. The VAWT's frontal area is represented as grey lines.
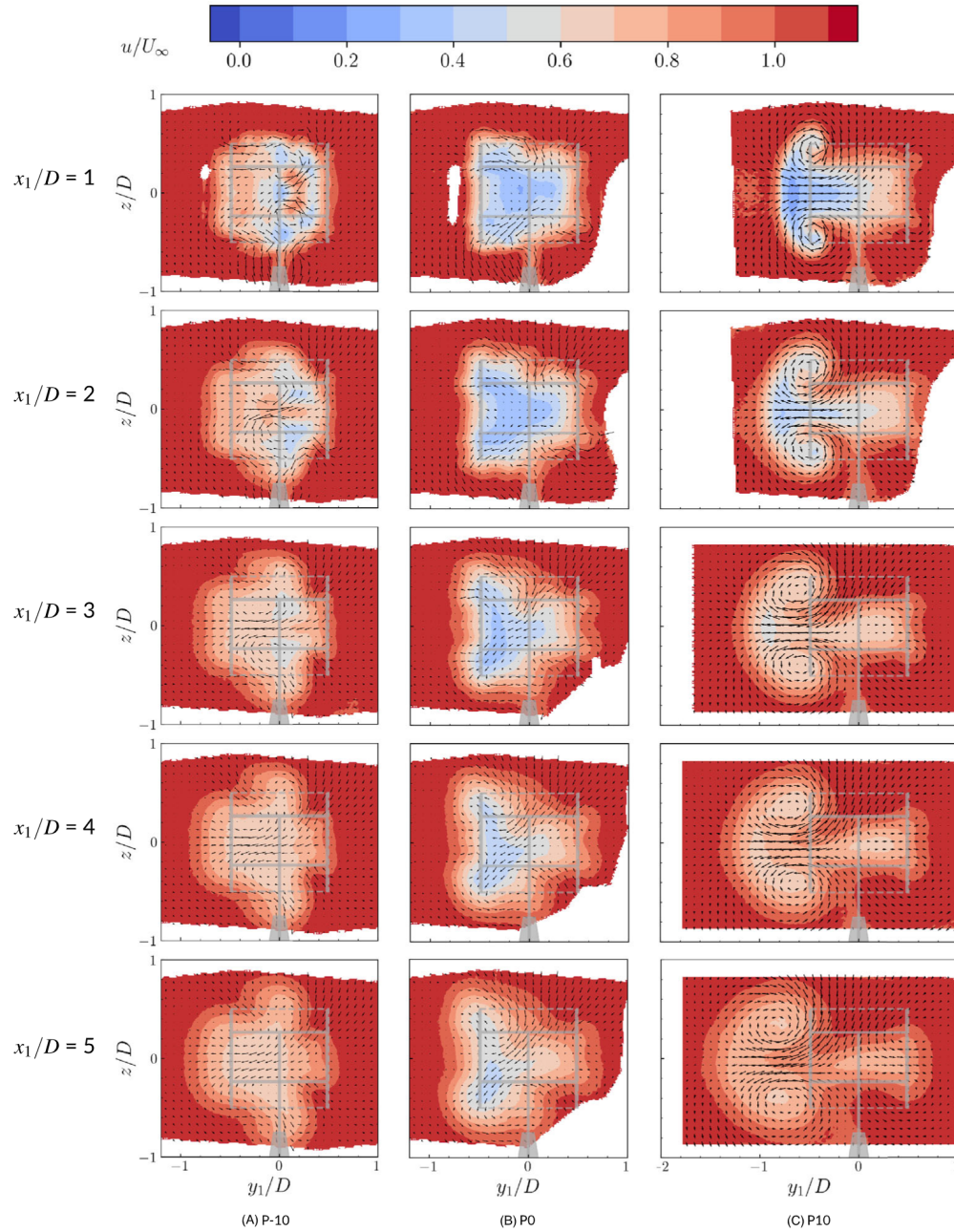
FIGURE A1 Streamwise velocity contours with in-plane velocity vectors for the isolated VAWT P$-$10, P0 and P10 at near wake ($x_1/D = 1, 2, 3, 4, 5$).
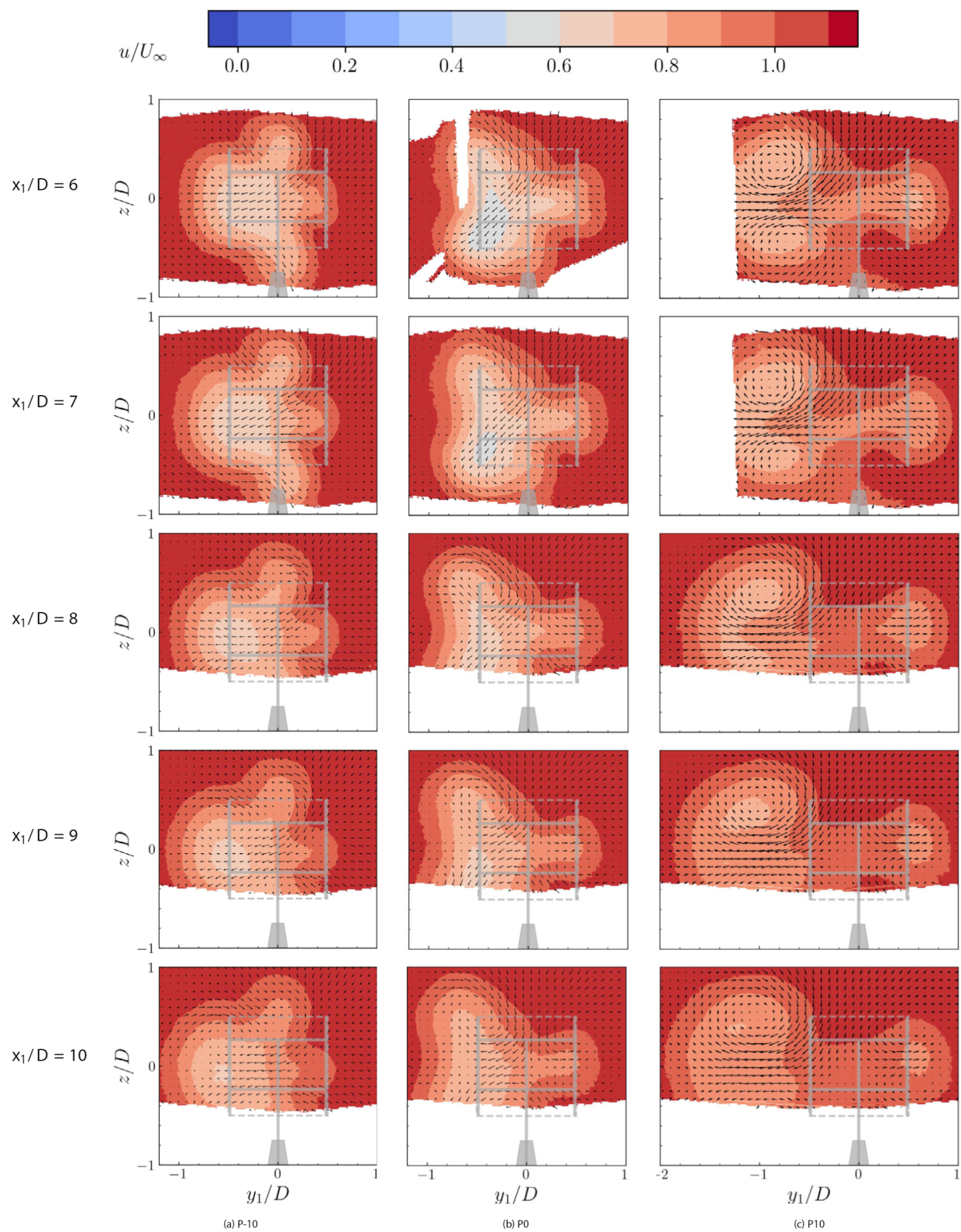
FIGURE A2 Streamwise velocity contours with in-plane velocity vectors for the isolated VAWT P−10, P0 and P10 at far wake ($x_1/D = 6, 7, 8, 9, 10$).

A.2 | Streamwise vorticity

The streamwise vorticity of the control group P−10, P0 and P10 are illustrated in Figures A3 and A4, where the in-plane streamlines are plotted to identify the location of streamwise vortices. The green contour line denotes the wake outline defined by $u/U_\infty = 1$.
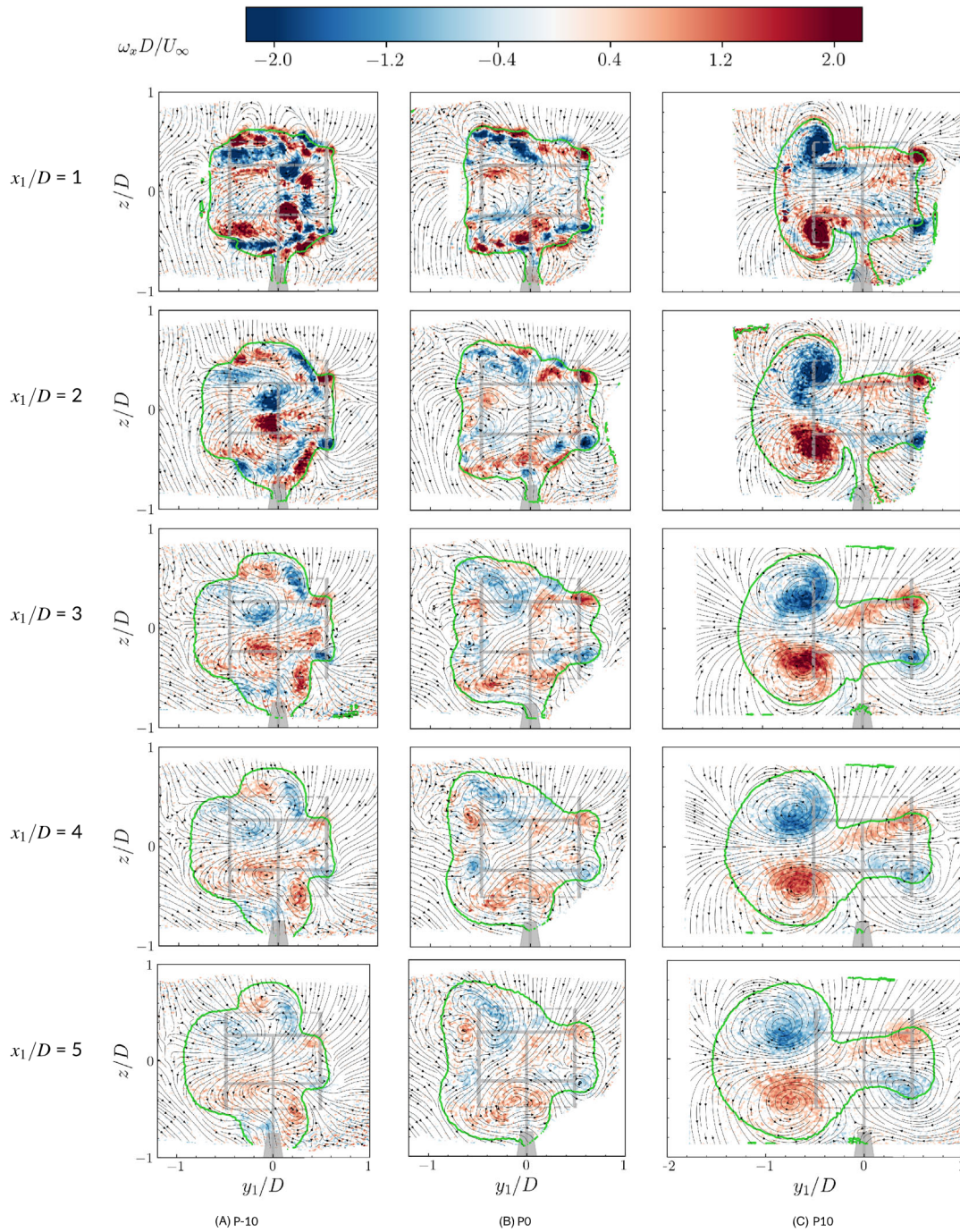

FIGURE A3 Streamwise vorticity contours with in-plane streamlines for the isolated VAWT P−10, P0 and P10 at near wake ($x_1/D = 1, 2, 3, 4, 5$). Green contour lines indicate $u/U_\infty = 1$.
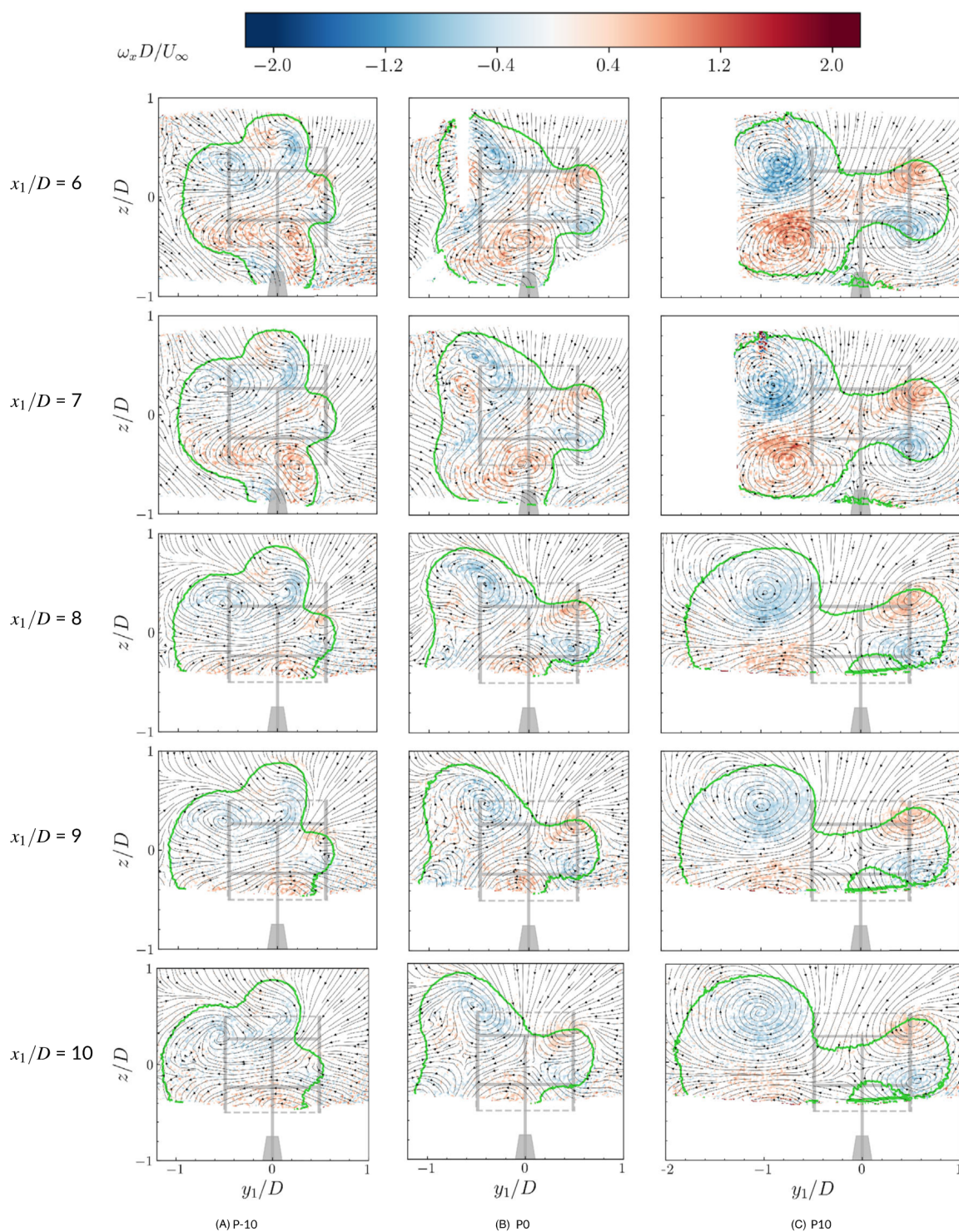
FIGURE A4 Streamwise vorticity contours with in-plane streamlines for the isolated VAWT P−10, P0 and P10 at far wake ($x_1/D = 6,7,8,9,10$). Green contour lines indicate $u/U_\infty = 1$.

A.3 | Turbulence intensity

The turbulence intensity in the wake of the control group P−10, P0 and P10 are illustrated in Figures A5 and A6,
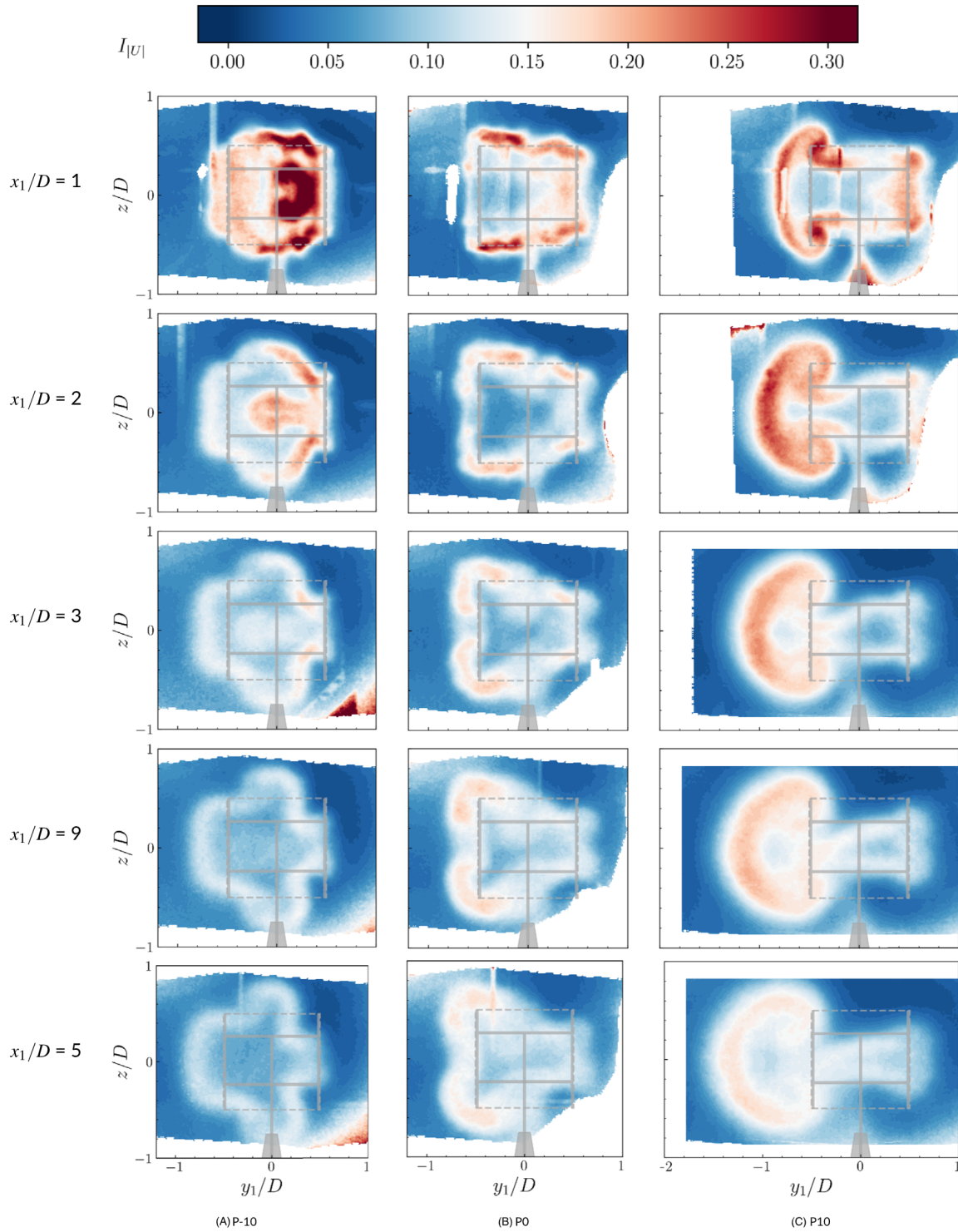

FIGURE A5 Streamwise turbulence intensity contours for the isolated VAWT P−10, P0 and P10 at near wake ($x_1/D = 1, 2, 3, 4, 5$).
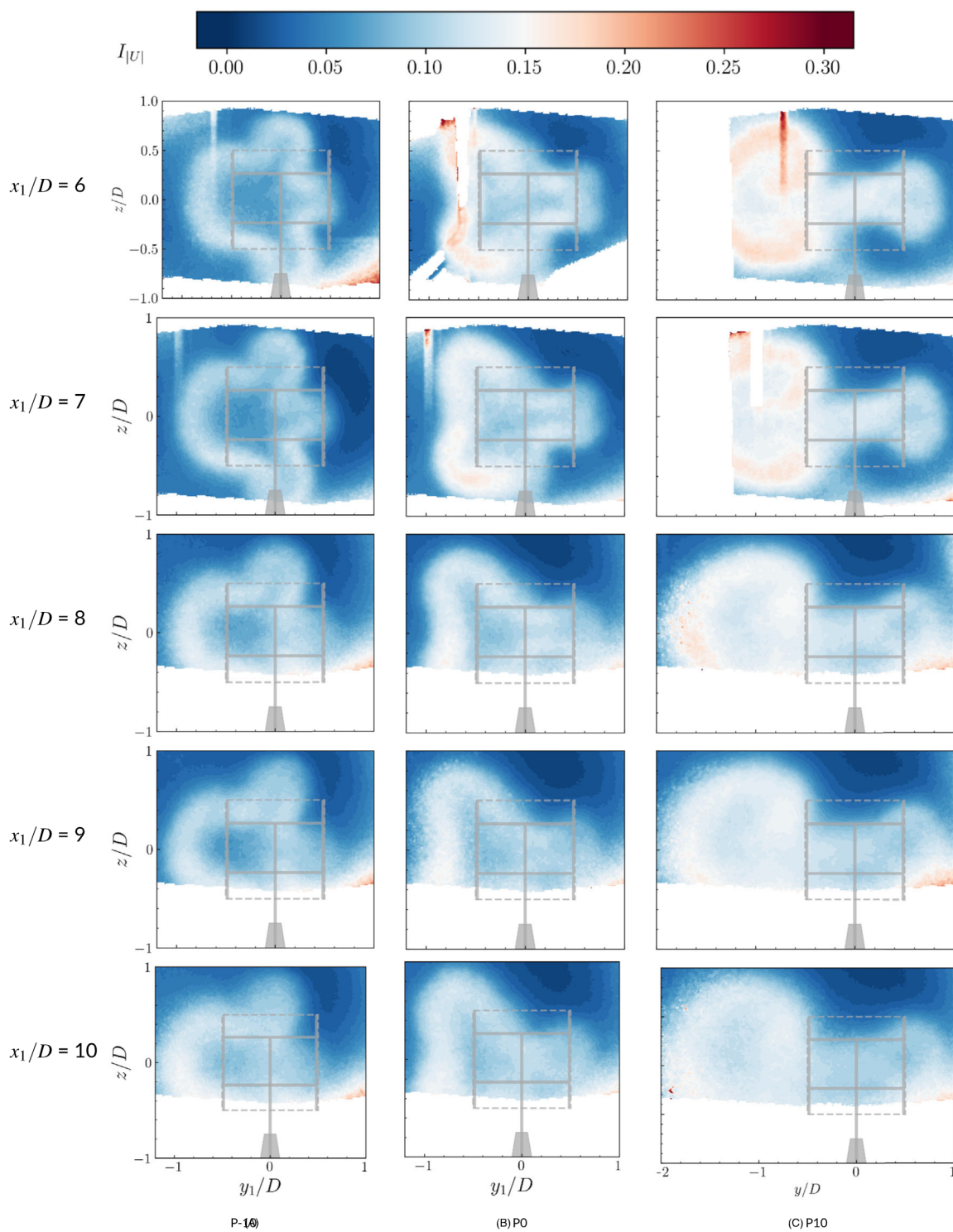
FIGURE A6 Streamwise turbulence intensity contours for the isolated VAWT $P-10$, $P0$ and $P10$ at far wake ($x_1/D = 6, 7, 8, 9, 10$).